JOURNAL OF GEOPHYSICAL RESEARCH: OCEANS, VOL. 118, 5353–5375, doi:10.1002/jgrc.20386, 2013

Assessing high-resolution analysis of surface heat fluxes in the Gulf Stream region

Xiangze Jin[1] and Lisan Yu[1]

Received 1 April 2013; revised 29 August 2013; accepted 1 September 2013; published 15 October 2013.

[1] A satellite-based global analysis of high-resolution (0.25°) ocean surface turbulent latent and sensible heat fluxes was developed by the objectively analyzed air-sea fluxes (OAFlux) project. Resolving air-sea flux down to the order to 0.25° is critical for the description of the air-sea interaction on mesoscale scales. In this study, we evaluate the high-resolution product in depicting air-sea exchange in the eddy-rich Gulf Stream region. Two approaches were used for evaluation, one is point-to-point validation based on six moored buoys in the region, and another is basin-scale analysis in terms of wave number spectra and probability density functions. An intercomparison is also carried out between OAFlux-0.25°, OAFlux-1°, and four atmospheric reanalyses. Results indicate that OAFlux-0.25° is able to depict sharp oceanic fronts and has the best performance among the six participating products in comparison with buoy measurements. The mean OAFlux-0.25° differences in latent and sensible heat flux with respect to the buoy are 7.6 Wm^{-2} (7.7%) with root-mean-square (RMS) difference of 44.9 Wm^{-2}, and 0.0 Wm^{-2} with RMS difference of 19.4 Wm^{-2}, respectively. Large differences are primarily due to mismatch in SST between gridded data and point measurements when strong spatial gradients are presented. The wave number spectra and decorrelation length scale analysis indicate OAFlux-0.25° depicts eddy variability much better than OAFlux-1° and the four reanalyses; however, its capability in detecting eddies with smaller scale still needs to be improved. Among the four reanalyses, CFSR stands out as the best in comparison with OAFlux-0.25°.

Citation: Jin, X., and L. Yu (2013), Assessing high-resolution analysis of surface heat fluxes in the Gulf Stream region, *J. Geophys. Res. Oceans*, *118*, 5353–5375, doi:10.1002/jgrc.20386.

1. Introduction

[2] Turbulent latent and sensible heat fluxes are important heat exchanges at the air-sea interface that influence and are influenced by atmospheric and oceanic processes on various temporal and spatial scales. One fundamental scale of variability in the oceans is the eddy-length scale. As shown by *Wunsch* [2002], oceanic kinetic energy is dominated by mesoscale eddies and the eddy kinetic energy tends to be greatest in places such as the western boundary currents and the Antarctic Circumpolar Currents where ocean fronts with sharp horizontal temperature gradients are featured. There has been ample evidence in literature that ocean mesoscale eddies and fronts modulate the marine meteorological boundary and exert great influence on air-sea exchanges of heat, moisture, and momentum [see a review by *Small et al*., 2008]. These out-of-ocean fluxes force an atmospheric response, and the impact can be well identified in the midtroposphere and beyond [*Sweet et al*., 1981; *Minobe et al*., 2008]. Climate study and oceanic research have entered the era of eddy permitting and/or eddy resolving. Air-sea fluxes are at the center of ocean-atmosphere interactions and their impacts. It is anticipated that the computation of air-sea fluxes with a resolution capable of resolving ocean mesoscale features would be important for improved characterization of air-sea interactions over ocean fronts and eddies.

[3] The length scale of mesoscale eddies ranges typically from 1000s km at low latitudes to 100s km at midlatitudes and down to 10s km at high latitudes [*Chelton et al*., 1998; *Small et al*., 2008; *Jiang et al*., 2012]. In general, the first baroclinic Rossby radius L decreases with increasing latitude; in the Gulf Stream (GS) region it is about 20–30 km [*Chelton et al*., 1998]. The wavelengths for the eddy variability can be estimated as $2\pi L$ [*Williams et al*., 2007]; thus, the correspondingly length scale is about 120–180 km. Therefore, one needs to use a flux product that has a resolution higher than one degree to resolve the features related to eddies and ocean fronts associated with the GS variability. Air-sea fluxes are presently computed from bulk flux parameterizations with surface meteorological variables from satellite retrievals and atmospheric reanalyses as inputs. Some satellite-derived surface heat flux analyses were constructed using spatial resolution of 0.25°

[1]Department of Physical Oceanography, Woods Hole Oceanographic Institution, Woods Hole, Massachusetts, USA.

Corresponding author: Dr. X. Jin, Department of Physical Oceanography, Woods Hole Oceanographic Institution, Mail Stop 21, Woods Hole, MA 02543, USA. (xjin@whoi.edu)

2169-9275/13/10.1002/jgrc.20386

[e.g., *Kubota et al*., 2002; *Shie et al*., 2012], some were based on 0.5° grids [e.g., *Andersson et al*., 2011], and some were binned onto 1° grids [e.g., *Bentamy et al*., 2003]. At the same time, atmospheric reanalyses have made efforts in improving surface fluxes through implementing improved parameterizations and finer resolution. The latest reanalyzed surface fluxes have a spatial resolution all between 0.3° and 0.7° [*Saha et al*., 2010; *Dee et al*., 2011; *Rienecker et al*., 2011], which improve considerably the previous versions that have a resolution much coarser than 1° [*Kanamitsu et al*., 2002; *Uppala et al*., 2005; *Kalnay et al*., 1996]. The authors of the present study are the developers of the objectively analyzed air-sea fluxes (OAFlux) project and have produced 50-plus years of global ocean evaporation and turbulent heat flux analysis by using an advanced objective analysis approach to find optimal representation of surface meteorological variables from multiplatform satellite retrievals and atmospheric reanalyzed fields [*Yu et al*., 2008]. Since the objective analysis takes into account data errors in synthesizing data from various sources and produces an estimate that has the minimum variance, the resulting flux analysis has improved accuracy [*Yu et al*., 2004a, 2004b; 2008]. However, the five-decade long OAFlux analysis was constructed on 1° grids, which is apparently not sufficient for resolving spatial scales of mesoscale variability.

[4] New efforts have been made to OAFlux to construct a higher-resolution (0.25°) turbulent latent and sensible heat flux analysis for the satellite era by taking advantage of several recent achievements obtained by individual research groups in improving the accuracy and quality of flux-related variables. Three data sets are particularly beneficial in developing the OAFlux-0.25° flux analysis. The first data set is the 0.25° analysis of near-surface air temperature and humidity derived from the advanced microwave sounding unit A (AMSU-A) and the Special Sensor Microwave Imager [*Jackson et al*., 2006, 2009; *Jackson and Wick*, 2010]. The second data set is the 0.25° analysis of global ocean vector winds from an objective synthesis of satellite sensors that consist of nine microwave passive radiometers, one polarimetric radiometer, and two scatterometers from QuikSCAT and ASCAT [*Yu and Jin*, 2012]. The third data set is a suite of fine-resolution products from the group for high resolution sea surface temperature (GHRSST). We selected the NOAA operational 25 km global SST based on the advanced microwave scanning radiometer-EOS (AMSR-E) and advanced very high resolution radiometer (AVHRR) [*Reynolds et al*., 2007]. The last two data sets are similar to what were used in constructing OAFlux-1° products, albeit the resolution is refined and quality is improved owing to the addition of sensors.

[5] This study will use the newly developed OAFlux-0.25° flux product to assess the advantages of high resolution in resolving air-sea exchanges on mesoscale variability in the GS region. The region is chosen because it is the site of intense air-sea interaction where strong turbulent latent and sensible heat loss contributed to larger total heat loss from the oceans, with the daily mean exceeding 1000 Wm^2 during a cold winter outbreak [*Cronin et al*., 2010; *Kelly et al*., 2010; *Weller et al*., 2012]. The region is also the site for a field program, namely, the CLIVAR mode water dynamics experiment (CLIMODE) that was designed to study the role of air-sea fluxes and ocean dynamics in the formation, evolution, storage, dispersal, and large-scale consequences of eighteen degree water (EDW), the subtropical mode water of the North Atlantic [*Marshall et al*., 2009]. One buoy was deployed during the CLIMODE project, which, together with five existing coastal station buoys operated by the National Data Buoy Center (NDBC) in the area, provides multiple in situ time series of surface meteorology and fluxes valuable for validation.

[6] The assessment analysis in this study aims to evaluate two aspects of the OAFlux-0.25° product, namely, the degree of improvement made to the accuracy of flux estimates and the degree of improvement made to the spatial-temporal flux variability associated with ocean fronts/eddies in the GS region. The six in situ buoys (i.e., CLIMODE plus five NDBC buoys) that are available in the area of interest provide valuable benchmark time series for evaluating the accuracy of temporal variability of gridded flux products at selected buoy sites, but are not sufficient to provide an integrated perspective of flux variability over the regional scale. Spatial-temporal variability is usually analyzed by statistical methods, such as wave number spectrum analysis [*Milliff et al*., 2004; *Vogelzang et al*., 2011] and spatial decorrelation length scale analysis [*Jiang et al*., 2012] to identify spatial representation scales in gridded products, and probability density functions (PDFs) analysis [e.g., *Gulev and Belyaev*, 2011] to examine error variances and the probability for extreme synoptic events. Hence, we combined buoy evaluation with the two above mentioned statistical methods to provide a more complete insight into the statistical aspects of the OAFlux high-resolution analysis. Given that the latest atmospheric reanalyses made substantial progress in surface flux estimates compared to the first-generation reanalyses, we included four reanalyses in the assessment analysis to gain an improved understanding of the state-of-the-estimation of the latest atmosphere reanalyzed surface fluxes in comparison with satellite-based OAFlux-0.25°. The four reanalyses flux products are the European centre for medium-range weather forecasts (ECMWF) Reanalysis Interim project (ERA-interim), the NASA's modern era retrospective-analysis for research and applications (MERRA), the National Centers for Environmental Prediction (NCEP) Climate Forecast System Reanalysis (CFSR), and the first generation reanalysis from the NCEP/National Center for Atmospheric Research (NCAR) Reanalysis.

[7] This paper is organized as follows. Section 2 provides a brief introduction to the six data products in use, including OAFlux-0.25°, OAFlux-1°, CFSR, ERA-interim, MERRA, and NCEP. A brief description of the six buoys (CLIMODE plus five NDBC buoys), including types of measurements and accuracy, is also given. The analysis of buoy evaluation of the six flux products is presented in Section 3. Characterizing the spatial and temporal representations of the six flux products in the GS region using statistical analysis of wave number spectrum, spatial decorrelation length scale, and PDFs is presented in Section 4. Summary and conclusions are given in Section 5.

2. Data

2.1. OAFlux-0.25° Versus OAFlux-1°

[8] The OAFlux-0.25° daily mean latent heat (LH) flux and sensible heat (SH) flux have been developed using a similar technique that was used in OAFlux-1° [*Yu et al*.,

2008]. A variational objective analysis method was applied to obtain the best estimates of flux-related surface meteorological variables through synthesizing satellites observations with reanalyses providing necessary supplementary data sets in case satellite observations are not available. The surface heat fluxes were then computed from the state-of-the-art COARE bulk flux algorithm 3.0 [*Fairall et al*., 2003].

[9] The flux-related surface meteorological variables that are optimized in OAFlux objective analysis include wind speed (U), near-surface air specific humidity (Qa), and temperature (Ta), sea surface temperature (SST), and sea surface pressure. Wind speed was taken from the newly developed OAFlux-0.25° satellite-based ocean vector winds analysis (1987 onward) [*Yu and Jin*, 2012] that was obtained through an objective synergy of 12 satellite sensors, including two scatterometers (QuikSCAT and ASCAT), nine passive microwave radiometers (AMSR-E, six SSM/I series and two SSMIS series), and the passive polarimetric microwave radiometer from WindSat mission. *Yu and Jin* [2012] evaluated the OAFlux-0.25° vector wind analysis at 126 moored buoy locations and reported that the mean difference between the high-resolution analyzed wind speeds and buoy measurements is -0.13 ms^{-1} and the root-mean-square (RMS) difference is 0.71 ms^{-1} based on 168,836 daily mean values.

[10] The 10 m Ta and Qa products derived from satellite retrievals by *Jackson et al*. [2009, 2010] were the primary data sets in OAFlux-0.25° analysis. *Jackson et al*. [2009, 2010] derived Ta and Qa at 10m from satellite retrievals of SSM/I, SSMIS, and AMSU using a multivariable linear regression. The data sets have a spatial grid resolution of 0.25°, covering the global oceans from 70°S to 70°N for the period of 1999–2010. The mean coverage of the data on daily basis over the GS region is about 80% (Figure 1). The coverage is lower in subtropics than over the midlatitudes because the orbital geometry tends to create more gaps at low latitudes. Over five out of six locations of the buoy used in this study the coverage is more than 85%. There is no data within 50 km of any coastline where the SSM/I data were contaminated by the abrupt change in surface emissivity between water and land. Note that compared to the satellite-derived wind speed, the coverage for Ta and Qa is relatively lower. The mean coverage of the daily mean satellite-derived wind speed is more than 97% over the global ice free ocean since July 1999 due to multiply sensors used in the analysis [*Yu and Jin*, 2012].

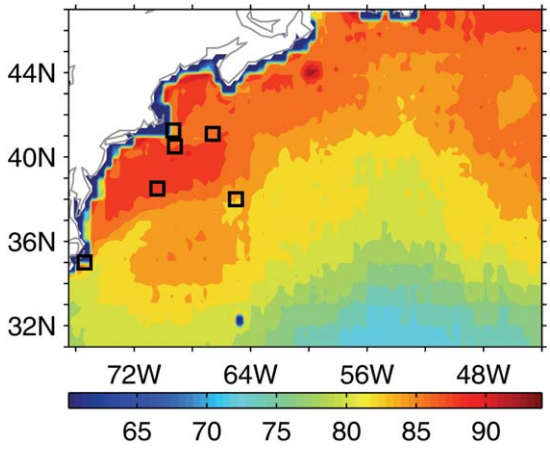

Figure 1. The mean percentage of the ocean areas covered by the corresponding satellite-derived 10 m specific humidity on daily basis for the period from 2002 to 2010. The squared black boxes denote the locations of the buoys used in the study.

[11] Compared to atmospheric reanalysis, the satellite-derived Ta and Qa data sets show much refined spatial variability on synoptic time scales. However, the data sets were not used directly; rather they were height adjusted to 2 m using the COARE algorithm [*Fairall et al*., 2003]. The estimates are biased when validated with buoys. In the tropics, there are wet biases in Qa estimates and warm biases in Ta estimates, while in the extra tropics, the signs of biases are reversed with dry biases in Qa estimates and cold biases in Ta estimates (not shown). The mean estimates were adjusted based on OAFlux-1° before being synthesized.

[12] SSTs were taken from the NOAA operational 25 km global SST based on AMSR-E [*Reynolds et al*., 2007]. Unlike OAFlux-1° that synthesizes satellite-derived SST with reanalyses SSTs to obtain optimal SST estimates, the OAFlux-0.25° analysis uses the reanalyses SSTs only as constraint for the synthesis of Ta and Qa, but not to reproduce OAFlux SST.

2.2. Surface Heat Flux Products From Four Reanalyses

[13] The four reanalyses (Table 1) used in this study are ERA-interim, MERRA, CFSR, and NCEP reanalysis. ERA-interim is a bridge between ERA40 and the next-generation extended reanalysis envisaged at ECMWF. The major advances in ERA-Interim include many model improvements, such as the use of four-dimensional variational analysis, a revised humidity analysis, improved bias correction for satellite data, and higher spatial and temporal resolutions. The ERA-interim surface variables are available at 3 h intervals at resolutions T255 (∼79 km or 0.703°) [*Dee et al*., 2011].

[14] MERRA is the NASA reanalysis for the satellite era (from 1979 onward) using a new version of the Goddard Earth Observing System Data Assimilation System (GEOS) atmospheric model v5.2.0 and data assimilation system (DAS). The project was aimed at improving the representation of the water cycle on a broad range of weather and climate time scales by assimilating the NASA Earth Observing System (EOS) series to improve cloud properties and moisture distribution. The resolution of GEOS atmospheric model is 1/2° latitude by 2/3° longitude with 72 vertical levels and is available at hourly temporal resolution [*Rienecker et al*., 2011].

[15] The recently completed CFSR is NCEP's third global reanalysis, and has many improvements in model functions and assimilation techniques over NCEP reanalysis and NCEP—Department of Energy reanalysis (NCEP2, not used in this study). The three main differences from the earlier NCEP efforts include higher horizontal and vertical resolution of the atmosphere (T382 L64), the use of a coupled atmosphere-ocean-land surface-sea ice system, and the assimilation of radiance measurements from

Table 1. List of Products Used in This Study, Including Spatial, and Temporal Resolution of Each Product

Acronym	Spatial Resolution	Sample Resolution and Temporal Coverage	References
CFSR	0.31°	Hourly, 1979–2009	*Saha et al*. [2010]
NCEP 1	1.875°	6 h, 1948 onward	*Kalnay et al*. [2006]
MERRA	0.5° (lat); 0.67° (lon)	Hourly, 1979 onward	*Rienecker et al*. [2011]
ERA-Interim	0.70°	3 h, 1979 onward	*Dee et al*. [2011]
OAFlux-1°	1°	Daily, 1958 onward (LH, SH, E, winds)	*Yu et al*. [2008]
OAFlux-0.25°	0.25°	Daily, 1999 onward (LH, SH, E) Daily, 1987 onward (winds)	*Yu and Jin* [2012]

historical satellites in addition to all conventional data [*Saha et al*., 2010]. The CFSR is caste as the successor of NCEP2, and will extend back to 1948; as such, it will be the successor of NCEP reanalysis. CFSR surface products are available at an hourly time resolution and 0.31° horizontal resolution.

[16] NCEP reanalysis has been available for many years. It represents the first efforts toward producing a comprehensive record of past atmospheric conditions using fixed, up-to-date data assimilating/forecasting system with T62 L28 resolution. The NCEP surface fluxes are available every six hours, on a Gaussian 192 × 94 grid (approximately 1.875° in longitude and latitude). As shown in Table 1, the horizontal resolution in the latest reanalyses ranges between 0.3° and 0.7°, which is clearly an improvement over the early reanalysis from NCEP at 1.875° resolution. In general, the latest reanalyses represent an improvement over the earlier reanalyses. In this study, we will include both the latest and the early reanalyses to assess the degree of improvements made in the air-sea turbulent heat fluxes associated with the ocean fronts.

2.3. Time-Mean Heat Flux Pattern Depicted by the Six Heat Flux Products

[17] A total of six flux products are used in the analysis, namely, OAFlux-0.25°, OAFlux-1°, ERA-interim, MERRA, CFSR, and NCEP. The analysis is based on the period from December 2002 to February 2010 except for CFSR, which is available up to the end of 2009. This period covers eight winter seasons (December-January-February). The winter-mean LH + SH patterns in the GS region depicted by the six participating flux products along with the winter mean position of the 18°C SST isotherm from the corresponding data source are shown in Figure 2. The location of the 18°C isotherm approximates the location of the northern wall of the GS [*Weller et al*., 2012], with maximum LH + SH values on the right-hand side over the core path of the GS that has higher SSTs. A close relationship of the oceanic latent and SH fluxes with the GS fronts is indicated.

[18] OAFlux-0.25° has a sharper and stronger LH + SH along the GS fronts among all the products. OAFlux-1° agrees with OAFlux-0.25° except that the mean structure is general smoother and the LH + SH maximum is about 50 Wm^{-2} weaker. The four reanalyses show a broad agreement with OAFlux-0.25° in the mean pattern but vary in details from one product to another in terms of the width and magnitude of the LH + SH front. CFSR stands out as the best comparison with the OAFlux-0.25° among the four reanalyses products, this is particularly interesting, given that the two products are independent. Both depict a well-defined LH + SH front with maximum values exceeding 500 Wm^{-2}. By comparison, ERA interim has a mean pattern similar to CFSR, albeit the peak magnitude over the core of the GS is weaker in east of 65°W. MERRA displays a smooth structure with a magnitude that is the weakest among all products. NCEP, which has the coarsest spatial resolution at 1.875°, shows a smoothest and broadest LH + SH front and a weakest association with the location of the 18°C NCEP SST isotherm. However, with the magnitude of the LH + SH maximum greater than 450 Wm^{-2}, NCEP fluxes are among the strongest.

[19] The year-to-year winter variability in LH + SH, depicted by the time evolution of its zonal mean, is large, as shown in Figure 3. All products have similar patterns, featuring large variances in latitudes of 35–42°N, which are the locations of the maximum LH + SH front. Within this latitudinal band, oceanic turbulent heat losses are particularly intense in January 2004, February 2007, December 2009 and the whole winter in 2010. Weak heat losses are most noted in the winter of 2008. The six products differ mostly in magnitude of variability. NCEP fluxes are strongest, followed by CFSR, OAFlux-0.25°, OAFlux-1°, and ERA-interim, with MERRA being weakest. The differences in magnitude of zonal averages reflect both the width and magnitude of the maximum LH + SH front depicted by the six products. The LH + SH maximum values in OAFlux-0.25° and CFSR are centered along a sharp front meandering with the 18°C SST isotherm, while the large LH + SH values in NCEP are wide-spread along the LH + SH front.

2.4. In Situ Observations

[20] Six buoys were selected. Note that buoy data serve as validation data sets, so that they are not assimilated in the OAFlux analysis. The buoy locations are marked in Figure 2, and the buoy measurement periods used in the study are listed in Table 2. The CLIMODE buoy lasted for about 15 months, from November 2005 to February 2007. The mooring site was at 38°N, 65°W, close to the central location of the climatological maximum of LH + SH (Figure 2). The surface mooring was instrumented with two sets of Air-Sea Interaction Meteorological Systems (ASIMET) that provide measurements of surface air-sea variables (e.g., air and sea temperature, relative humidity, wind speed and direction, barometric pressure, downward short and longwave radiation, and rainfall) at a one minute sample rate. Buoy air-sea fluxes of heat, freshwater, and momentum are estimated using bulk flux formula. Typical accuracy of the derived buoy fluxes is about 5 Wm^{-2} (5%) and 2 Wm^{-2} (15%) for LH and SH, respectively [*Colbo*

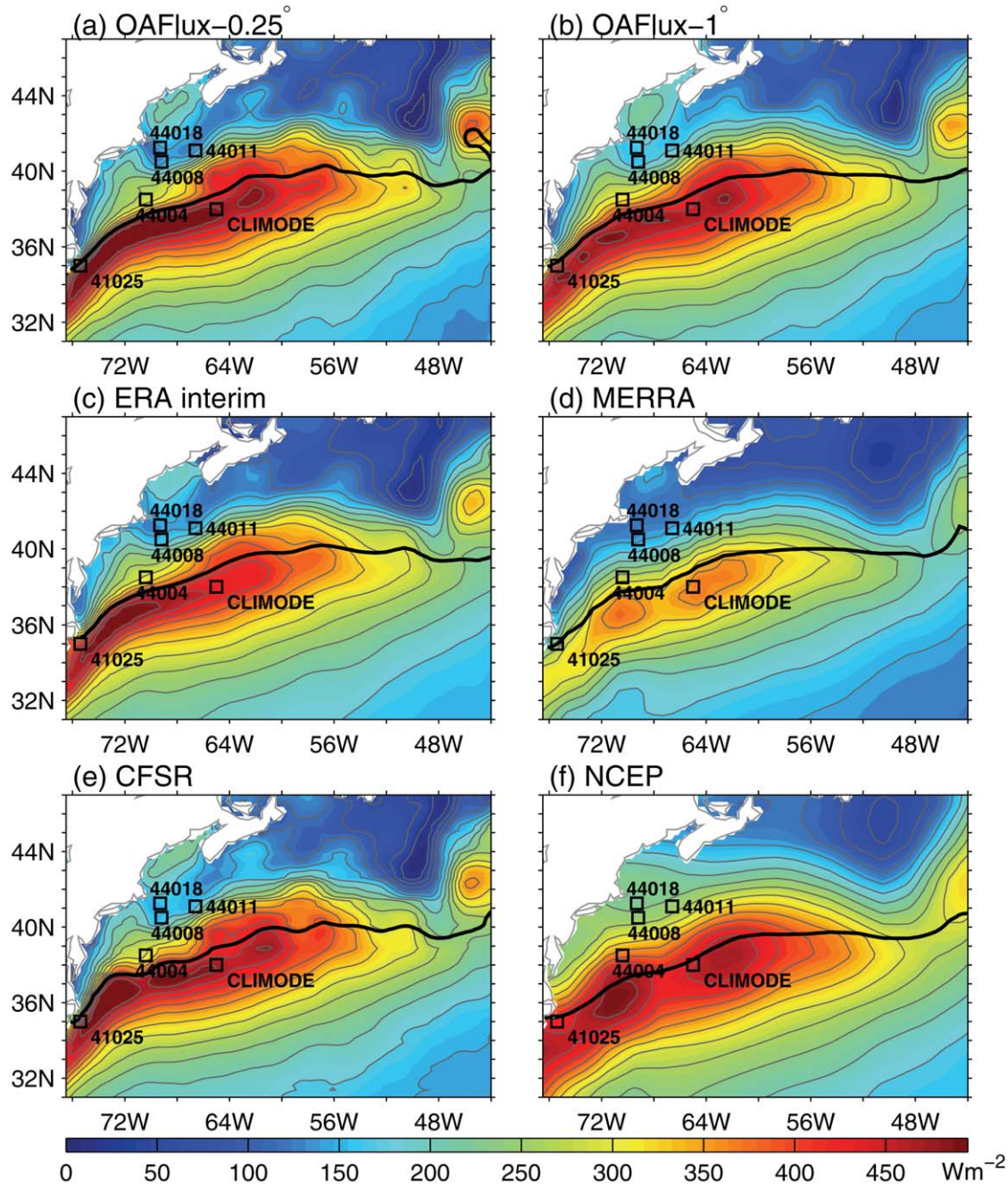

Figure 2. Winter-mean LH + SH in the Gulf Stream region from (a) OAFlux-0.25°, (b) OAFlux-1°, (c) ERA interim, (d) MERRA, (e) CFSR, and (f) NCEP1. The mean patterns were constructed from eight winters (December to February) for the period from December 2002 to February 2010. Positive values denote turbulent heat transfer from the ocean to the atmosphere (i.e., oceanic heat loss). Thick black curve in each plot denotes the location of the winter-mean 18°C SST isotherm from the corresponding data source. The six squared black boxes denote the locations of the six buoys used in the study, and the numbers denote the NDBC station numbers and CLIMODE denotes the field program.

and Weller, 2009]. In the GS location, it is anticipated that the uncertainties could be slightly larger due to harsh environmental conditions [*Bigorre et al*., 2013]. A detailed documentation of the CLIMODE buoy design, measurements, and accuracy can be found from *Weller et al*. [2012].

[21] The other five buoys are the offshore moored stations owned and maintained by NOAA's NDBC. Hourly measurements were recorded and transmitted, including wind speed, direction, gust, barometric pressure, air and sea temperature, relative humidity, and wave energy spectrum. Using these surface meteorological measurements, LH and SH can be computed using bulk flux formula. The locations of the five buoy stations compliment the CLIMODE buoy location, which together offer some spatial

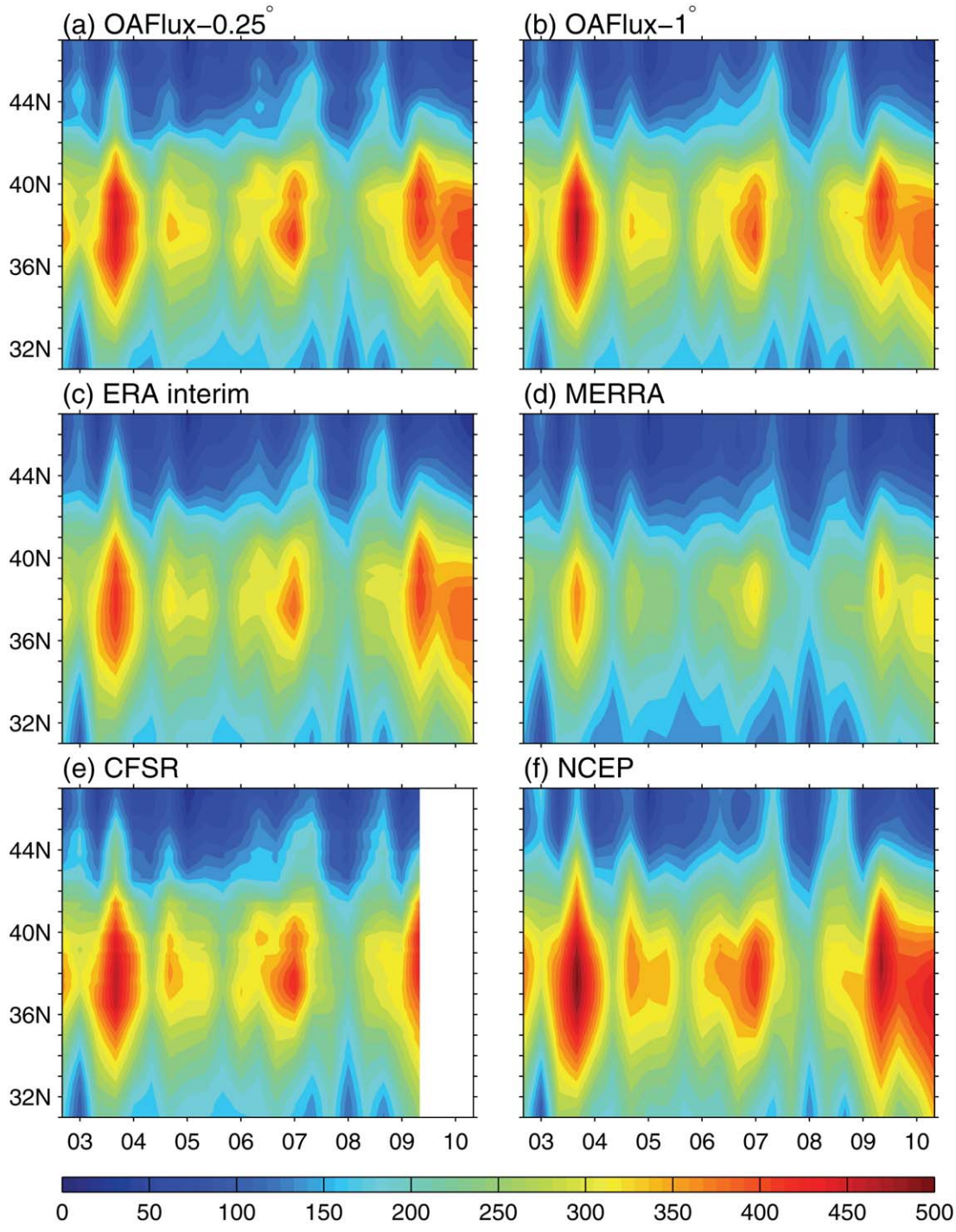

Figure 3. Time evolution of zonally averaged monthly mean LH + SH for the winter season (December to February) during the period from December 2002 to February 2010. Note that CFSR is available up to December 2009.

dimension of LH and SH variability in the GS region. Stations 41025 (75.4°W, 35.0°N) and 44004 (70.4°W, 38.5°N) are slightly off the elongated climatological maximum center of LH + SH (Figure 2), while stations 44,008 (69.2°W, 40.5°N), 44,011 (66.6°W, 41.1°N), and 44,018 (69.3°W, 41.3°N) are in the cold water region on the offshore side of the GS. Turbulent fluxes derived from NDBC buoys may be less reliable than data collected by scientifically oriented field experiments as the sensors selected by NDBC are less expensive, less accurate than those used for field experiments [*Bourras*, 2006]. The accuracy of the NDBC sensors (i.e., ARES Payload installed at each selected buoy in this study) are 10% for wind speeds, 3% for relative humidity, 1°C for Ta, and 1°C for SST [*National Data Buoy Center*, 2013]. By comparison, the accuracy of ASIMET are 5% for wind speed, 3% for relative humidity, 0.2°C for Ta, and

Table 2. List of Buoy, Location, Record Interval, and the Actual Time Period Used in This Study

Buoys	Location	Actual Period Being Used	Record Interval (min)
CLIMODE	38.0°N, 65.0°W	11/14/05 to 02/08/07	1
NDBC 41,025	35.0°N, 75.4°W	01/01/05 to 12/31/07	60
NDBC 44,004	38.5°N, 70.4°W	01/01/05 to 12/31/07	60
NDBC 44,008	40.5°N, 69.2°W	01/01/05 to 12/31/07	60
NDBC 44,011	41.1°N, 66.6°W	01/01/05 to 12/31/07	60
NDBC 44,018	41.3°N, 69.3°W	01/01/05 to 12/31/07	60

0.1°C for SST in calm environmental conditions [*Colbo and Weller*, 2009].

3. Buoy Evaluation

[22] Two adjustments were made to buoy measurements before they were used for evaluation. One was the height adjustment for buoy air temperature and humidity measurements. The CLIMODE instruments measured air temperature and relative humidity at a height of 2.7 m above the mean water line, while the instruments on the five NDBC buoys measured air temperature and relative humidity measurements at 4 m above site elevation. The gridded products from OAFlux and atmospheric reanalyses provide air temperature and humidity at 2 m. We chose 2 m as the standard height for these two variables in this study and adjusted the buoy measurements to 2 m using the COARE algorithm [*Fairall et al*., 2003]. The other adjustment was the equivalent neutral wind adjustment made to both buoy and atmospheric reanalyzed winds. The CLIMODE buoy wind measurements were made at a height of 3.4 m, while NDBC buoy winds were at 5 m. The winds from atmospheric reanalyses were all at 10 m but differ from OAFlux analyzed winds in that the latter are 10 m neutral winds. We applied an equivalent neutral wind conversion of *Liu and Tang* [1996] to reanalyzed winds and buoy winds and applied height adjustment to 10 m for the buoy winds the COARE algorithm. The daily-mean buoy data were used for validation.

3.1. Evaluation of OAFlux-0.25°

[23] Mean and daily variability of LH and SH estimates from OAFlux-0.25° are first examined using high-quality CLIMODE buoy measurements. Figures 4a–4f show the daily time series comparison of surface heat fluxes (i.e., LH and SH) and flux-related variables (i.e., SST, wind speed at 10 m, specific humidity and air temperature at 2 m) between OAFlux-0.25°and the CLIMODE buoy for the 15 month buoy measurement period from 14 November 2005 to 8 February 2007. Daily variability of OAFlux-0.25° analyzed fluxes and basic variables agrees generally well with that of buoy counterparts, except for the winter season in 2006, during which OAFlux-0.25° basic variables, most noted in SST and wind speed (Figure 4c), have a mean state evidently higher than that of the buoy measurements.

[24] The mean difference is 47.6 Wm^{-2} for LH and 14.8 Wm^{-2} for SH, and the RMS difference is 86.2 Wm^{-2} for LH and 36.1 Wm^{-2} for SH. Most of the RMS differences occurred during the winter seasons when the gridded SST and U estimates were higher than buoy measurements. Correlation coefficients between OAFlux-0.25° and buoy counterparts are all 0.87 and higher, and are significant at 95% confidence level. Qa and Ta have the highest correlations, both at 0.99, while U and SST have a correlation coefficient of 0.88 and 0.91, respectively. LH and SH have a respective correlation coefficient at 0.87 and 0.91, reflecting the combined influence of SST and wind speed.

[25] The OAFlux SST, which is the OISST 0.25° daily analysis derived from the AMSR-E and AVHRR, deviated from buoy SST by as much as 5°C between January and March 2006, during which buoy SST underwent rapid cooling and large synoptic variability whereas the satellite-based SST had a relatively weak cooling and weak synoptic variability. This SST discrepancy between the buoy measurements and satellite-derived product is due to the fact that buoy observations are quite sensitivity to the position of GS; on the other hand, satellite observations is less sensitive to the position of GS at this relatively low resolution. *Davis et al*. [2013] reported that, during the 15 month CLIMODE mooring period, the position of the buoy relative to the GS north wall was not fixed but changing, because the GS fluctuates with time. It was found that the buoy was located to the north (south) of the GS north wall ~55% (45%) of the time during the ~15 month record. The GS north wall is usually perceived as an open ocean barrier that separates the continental shelf waters from the warm interior waters of the GS and defines the location of sharp SST gradients (Figure 2). Hence, SST would be lowered down considerably if the buoy veered off to the north of the GS north wall in the maximum SST gradient zone. It is striking to see that the significant SST discrepancies between OAFlux-0.25° and buoy all occurred when the buoy was located north of the GS north wall.

[26] When comparing OAFlux gridded products with buoy measurements, one should know that buoy measurements are single point in situ measurements, while the OAFlux-0.25° estimates at each grid point represent the spatial averages over about 25 × 25 km^2 areas. Therefore, OAFlux-0.25° estimates at the CLIMODE buoy site are the results of the 25 × 25 km^2 area average in the neighborhood of the buoy site. At this resolution, the strong fronts cannot be clearly resolved, and the results obtained from the buoy in situ observations and the area-averaged satellite measurement can be different. For buoy-based SST comparison, if there are no dense SST gradients within 25 km diameter surrounding the buoy site, the area average is close to the single point measurements; otherwise, the

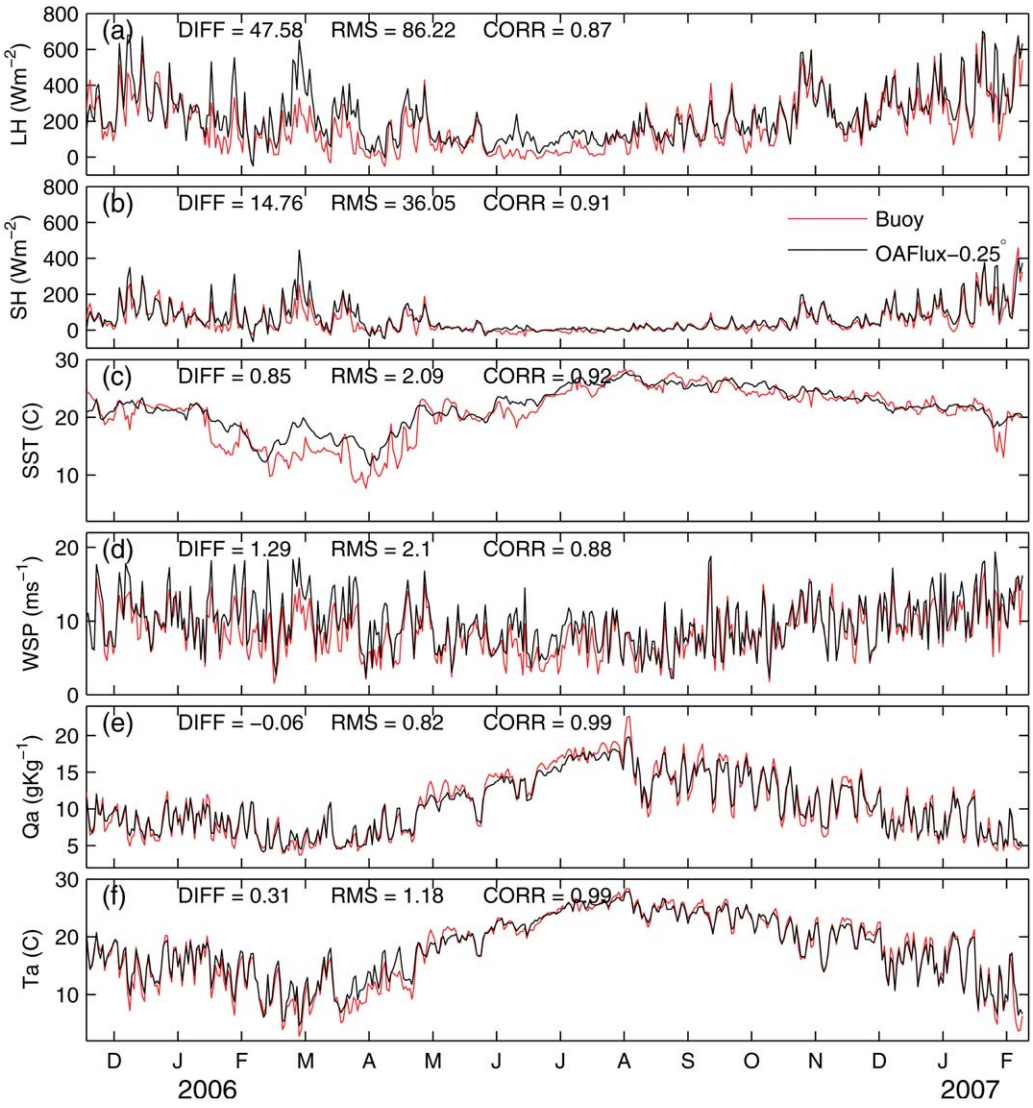

Figure 4. Time series comparison between OAFlux-0.25° daily mean variables (black lines) and CLIMODE buoy (38.0°N, 65.0°W) counterparts (red lines) for the buoy period from November 2005 to February 2007. (a) LH, (b) SH, (c) SST, (d) wind speed at 10 m, (e) specific humidity at 2 m, and (f) air temperature at 2 m.

difference between the two different representations can be large. Strong SST front can appear around the CLIMODE buoy site during the winter season. When the buoy is north of the GS north wall, buoy SST is rather low. On the other hand, the area-averaged SST includes the contribution of some warm GS waters. As a result, the area-averaged SST at the buoy site can be much warmer. This could be the reason that the satellite-based gridded SST product was higher than buoy SST in the winter season when the buoy was off the core of the GS front. During late summer (July-August-September) when the SST gradients are much weaker, the differences between the two SST representations are visibly small. This strengthens the argument here that the changing SST state around the buoy site affects the degree of comparison between the area average and point measurement.

[27] OAFlux-0.25° also shows stronger wind speed during the winter season when compared to buoy wind measurements. We suspect that the leading cause of the stronger-than-buoy winds might also be the difference between area average and point measurement. Wind speeds are enhanced over the GS fronts due to strong warm SST modulation on the marine atmospheric boundary layer stability that leads to the momentum aloft to be mixed down to the surface and increases the surface winds [*Wallace et al*., 1989; *Small et al*., 2008]. Buoy wind speed would be weaker when the buoy was north of the GS north wall, which was the case during January to March 2006. The 25 km × 25 km area averaged wind speed would reflect the average over a gradient zone of wind speed, which would be stronger.

[28] Hence, the difference between area average and point measurement is likely a major cause of large RMS differences between the gridded products and buoy fluxes. The presence of an ocean front puts a stringent condition in

obtaining a fair comparison for a gridded product with in situ buoy measurements.

[29] To examine the impact of spatial resolution on discrepancies between OAFlux and buoy measurement, we convert the 0.25° OAFlux SST data to a data set with 1° resolution for comparison (Figure 5). This figure shows that the 1° SST further underestimates the rapid cooling between January and March 2006, with the RMS difference increasing from 2.09 to 2.23°C. The SST from OAFlux-1° is also included as an independent data set, which seems smoother and has larger RMS difference compared to the 1° SST. Note that the OAFlux-1° SST is the AVHRR and reanalyses combined product, whereas the OAFlux-0.25° SST is the AVHRR and AMSR-E combined analysis, of which the primary AVHRR contribution is in regions near land where AMSR is not available. The AMSR-E and AVHRR SST has improved spatial resolution compared with the AVHRR-only product. In fact, especially in the western boundary current regions in winter clouds are often generated at a SST front, so that the AVHRR high-resolution infrared (IR) satellite measurements are not available. On the other hand, the IR spatial resolution is much better than microwave when skies are clear [*Chelton and Wentz*, 2005; *Reynolds et al*., 2007].

[30] To quantify the relative contribution of each meteorological variable to the errors in LH and SH, we linearize the bulk formula and decompose the basic variables onto the buoy mean and the deviations from the buoy mean. The following two relationships are obtained:

$$LH' \approx LH\left(\frac{U'}{U'U}+\frac{Q_s'}{Q_s-Q_a}+\frac{-Q_a'}{Q_s-Q_a}\right) \quad (1)$$

$$SH' \approx SH\left(\frac{U'}{U}+\frac{SST'}{SST-T_a}+\frac{-T_a'}{SST-T_a}\right) \quad (2)$$

where *LH, SH, U, Qs, Qa, SST* and *Ta* are buoy measurements of daily mean LH flux, SH flux, wind speed, saturation specific humidity, specific humidity, SST and air temperature, respectively. These variables with a prime (e.g., LH′) denote the differences between OAFlux-0.25° and buoy (i.e., OAFlux minus buoy). The right-hand side of equation (1) has three terms, representing the contributions of the OAFlux-buoy differences in wind speed (the first term, hereafter LH (U′)), saturation specific humidity (the second term, hereafter LH (Qs′)), and specific humidity at 2 m (the third term, hereafter LH (Qa′)) to the OAFlux-buoy differences in LH. Since Qs is determined by SST, LH (Qs′) is equivalent to LH (SST′). The right-hand side of (equation (2)) has the similar three terms, namely, SH (U′) (the first term), SH (SST′) (the second term), and SH (Ta′) (the third term).

[31] Time series of daily mean LH′ and the three contributing sources are shown in Figure 6a. It can be seen that LH (Qs′), or the equivalent LH (SST′) has the leading contribution to LH′, followed by contribution from LH (U′). It is estimated that LH (SST′) accounts for 49.3% of variances in LH′, LH (U′) accounts for 18.3%, and LH(Qa′) accounts for 11.7%. The SH′ and the three contributing terms are included in Figure 6b; this figure shows that SH (SST′) accounts for 77.8% of variances in SH′, SH (U′) accounts for 20.9%, and SH (Ta′) accounts for 26.2%. The SH (SST′) and SH (Ta′) combined together accounts for 44.8%, so that the corresponding variance is smaller than SH (SST′) alone because SST and Ta are closed linked. Clearly, the overestimated LH and SH in OAFlux are primarily caused by a warm bias in SST, which is further enhanced by a positive bias in wind speed. The bias of SH is partially offset by warm bias of air temperature.

[32] Figures 7–11 show the time series comparison of the other five products with respect to CLIMODE buoy. OAFlux-1° overestimates LH and SH by 43.4 Wm^{-2} and 12.8 Wm^{-2}, respectively; such errors are due to a warm SST and a strong wind bias (Figure 7). Compared to OAFlux-0.25°, OAFlux-1° has higher RMS difference and lower correlation coefficient in all fluxes and flux-related variables with respect to the buoy observations. Note that the mean bias for OAFlux-1° is relatively lower in both LH and SH, although it's corresponding SST is warmer than OAFlux-0.25°. By considering the mean difference in Qa (∼0.08 g/kg) and Ta (∼0.21°C) between the two products, the impact of warm bias in SST is offset by a warm bias in air temperature and a wet bias in humidity.

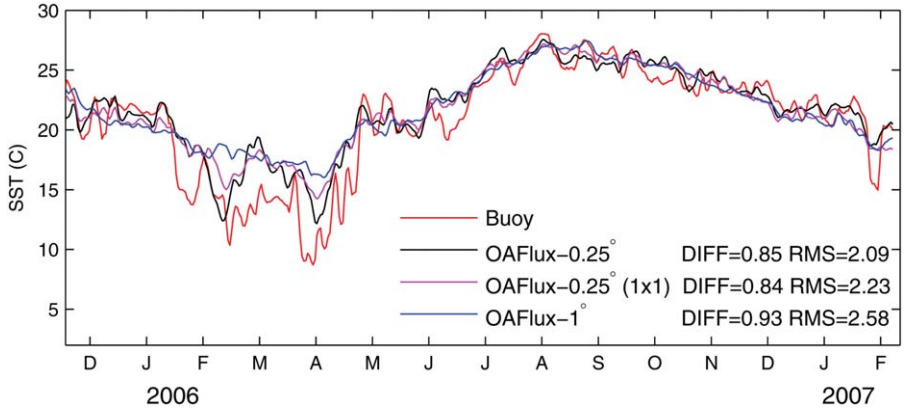

Figure 5. Time series comparison of SST between OAFlux-0.25°, 16-point area mean OAFlux-0.25° (1 × 1), OAFlux-1°, and CLIMODE buoy. A 3 day running mean was applied.

[33] Examination of the time series of ERA interim indicates that the reanalysis product shares similar quality as OAFlux-0.25° at CLIMODE (Figure 8). Compared to OAFlux-0.25°, ERA interim has warmer biases in both SST and Ta, but smaller bias in wind speed. The mean biases of Qa for the two products have opposite signs. The time series of CFSR shows that compared to OAFlux-0.25°, the reanalysis has smaller bias in Qa and wind speed but larger bias in Ta (Figure 9). Although the reanalysis has lower mean SST than OAFlux-0.25°, it has even bigger overestimates of LH, with the mean bias of 54.1 Wm^{-2}. This implies that the bias in LH is partially caused by the difference between the COARE algorithm and the bulk flux algorithm used in the reanalysis.

[34] Among the six products, MERRA has the smallest mean bias in both LH and SH against buoy observations. For example, the mean bias in LH is 20.3 Wm^{-2}, about 50% less than OAFlux-0.25°. However, compared to OAFlux-0.25°, it has very similar RMS difference and lower correlation coefficient. The time series of the four flux-related variables from MERRA show that there are significant biases in SST, Qa, and Ta (Figure 10), except for wind speed, which agrees well with buoy observations in general. SST appears to be overly smoothed and is much warmer than observations, with the mean bias of 1.58°C and RMS difference of 3.04°C. On the other hand, both Qa and Ta are significantly overestimated. The mean bias in Qa is 1.25 g/Kg, with RMS difference of 1.55 g/kg; the mean bias in Ta is 1.31°C, with RMS difference of 1.96°C. It is evident that high Qa and Ta help offset ocean heat loss caused by warm SST bias, and reduce the mean bias; however, they do not seem to reduce RMS difference much because both SST and Qa (or Ta) have significant biases against buoy observations.

[35] Time series of NCEP further confirms that SST is the least accurate variable among the four flux-related variables, in comparison with buoy counterparts (Figure 11). For the five data sets (OAFlux-1°, ERA interim, CFSR, MERRA, and NCEP) SST accounts 65.2, 70.1, 41.2, 101, and 52.3% of the total variance of LH′, respectively; and it accounts for 88.2, 115, 79.1, 150, and 58.6% of total variance of SH′. Because SST is closely linked to Ta and Qa, the variance of SST or Qs is larger than the variance of (SST-Ta) or (Qs-Qa). This accounts for the values >100%.

[36] Time series comparison of OAFlux-0.25° fluxes with the other five NDBC buoys obtained similar results that SST is the major cause of the deviations of the gridded LH and SH from the buoy fluxes. One example of using NDBC buoy Station 41025 for comparison is shown in Figure 12. This buoy is also located near the core of the GS front (Figure 2) but in the upstream of the CLIMODE buoy site. Although the buoy has time series dated back to year 2003, only the period from January 2006 to December 2007 that overlaps with the CLIMODE measurement period is used here. Daily variability of the LH and SH from OAFlux-0.25° compares well with buoy fluxes, with a correlation coefficient of 0.91 and 0.94, respectively. The gridded LH (SH) has a mean difference of 0.8 Wm^{-2}

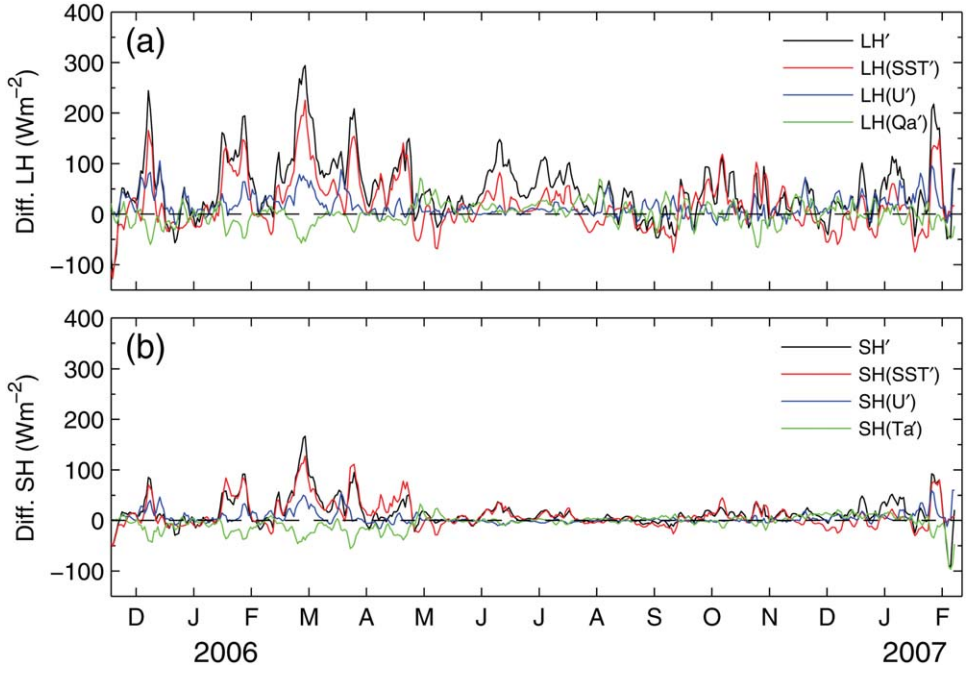

Figure 6. Time series of daily-mean differences between OAFlux-0.25° and CLIMODE (LH′) and the contribution from each basic variables (see equations (1) and (2) for details). (a) LH′ (black), LH(SST′) (red), LH(U′) (blue), and LH(Qa′) (green), and (b) SH′ (black), SH(SST′) (red), SH(U′) (blue), and SH(Ta′) (green). A 3 day running mean was applied.

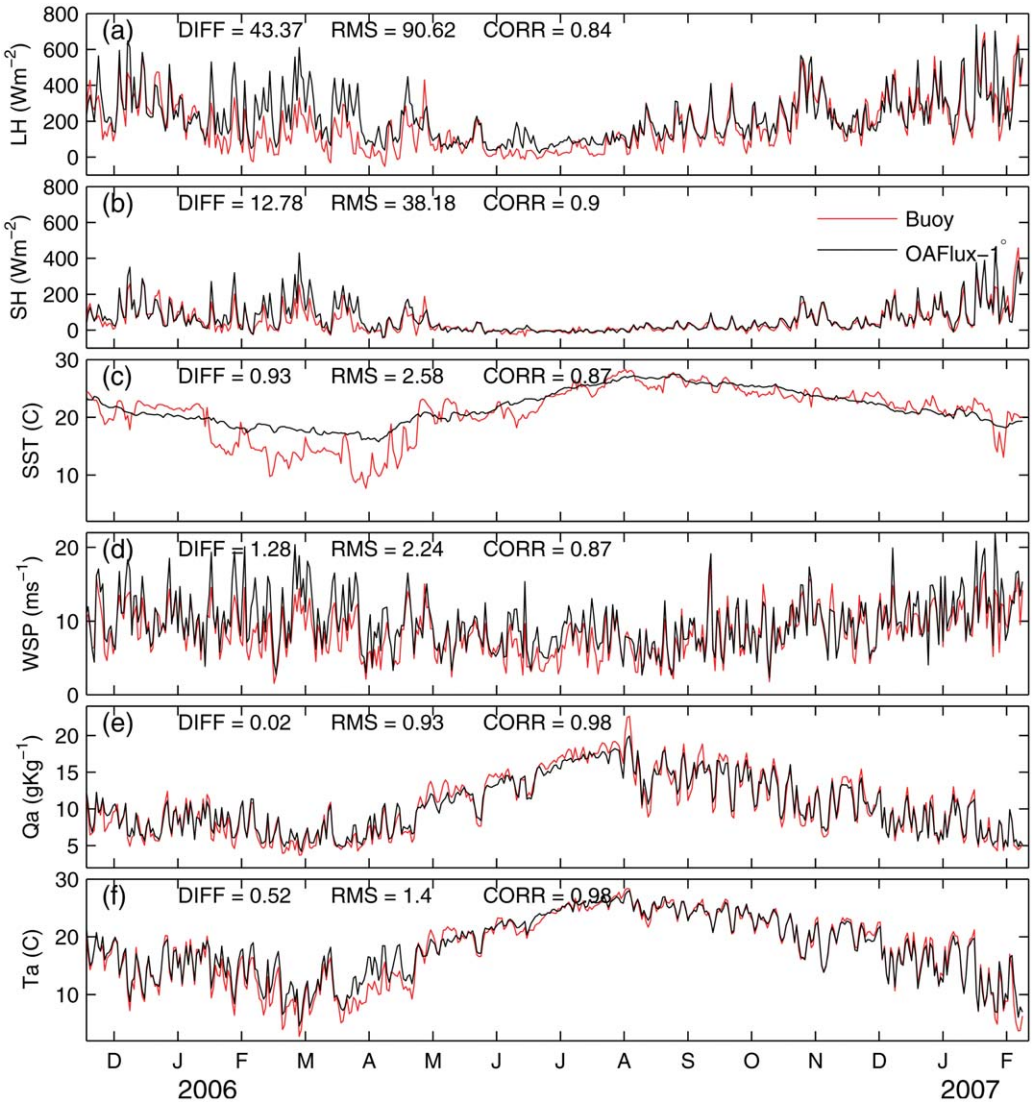

Figure 7. Same as Figure 4 but for OAFlux-1°.

(3.5 Wm^{-2}) and an RMS difference of 61.4 Wm^{-2} (23.5 Wm^{-2}). Comparisons of U, Qa, and Ta also show good agreement between OAFlux-0.25° and the buoy. However, significant mean departure of gridded SST from buoy SST is evident, particularly during the winter and early spring seasons. The SST being the leading cause of the RMS differences of LH is also found at this location, and the difference between area average and point measurement seems again to be the cause of the SST difference between the gridded data and buoy measurements.

3.2. OAFlux-0.25° Versus OAFlux-1°

[37] The annual mean (2003–2010) LH and SH from OAFlux-0.25° and the difference between OAFlux-0.25° and OAFlux-1° are shown in Figure 13. In making the difference plot, the 1° OAFlux data set is linearly interpolated into the 0.25° grids. Major differences in the two sets of LH annual means appear to be closely associated with the GS fronts, with the maximum difference exceeding 40 Wm^{-2} in a narrow zone located to the right-hand side of the GS north wall. It is evident that the low-resolution underestimates the peak heat loss from the oceans over the front. Away from the front, the differences between the two OAFlux products are generally small except for some localized eddy-like features along the GS northern extension, suggesting that the spatial resolution does not change the mean pattern of surface heat flux but does change detailed depiction, such as peak magnitude and structure, of surface fluxes in the vicinity of ocean fronts and eddies. A similar difference pattern between the two OAFlux LH products is also seen when comparing the mean fields constructed for the winter seasons only, except that the LH differences over the GS front have a much larger magnitude. This is anticipated as the annual-mean surface flux pattern in the GS is primarily determined by the strong air-sea exchanges during the fall-winter seasons. The same arguments apply to the two SH products from OAFlux. The difference pattern in the annual-mean SH is similar to that of

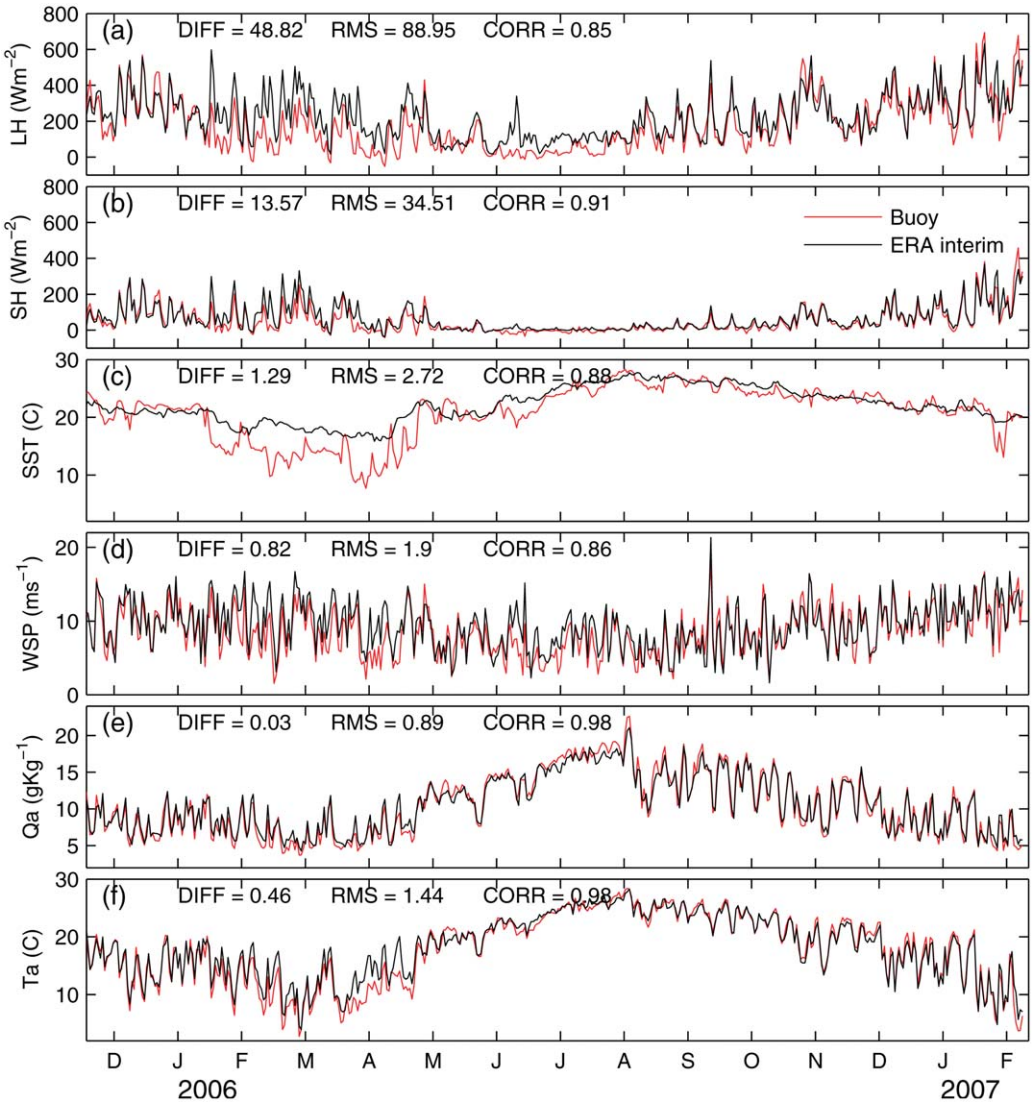

Figure 8. Same as Figure 4 but for ERA interim.

the LH difference pattern, but the magnitude is comparably weaker, not exceeding 20 Wm^{-2}.

3.3. OAFlux Versus Reanalyzed Fluxes

[38] The daily mean variability of LH and SH from six products, including two OAFlux products and four atmospheric reanalyzed flux products (Table 1) was evaluated using the six participating buoys based on three basic matrices: the mean average over the available or targeted buoy measurement period (Table 2), RMS of the differences between product and buoy, and correlation between product and buoy. Figures 14a and14b show the comparison of the mean averages of LH and SH from the six products with buoy counterparts at the six buoy locations. In terms of the relative location of each buoy to the GS front varies, the six buoys can be loosely clustered into two groups, named group-warm and group-cold, based on their proximity to the location of the GS north wall (e.g., the SST 18°C isotherm in Figure 2). The group-warm include the three buoys, CLIMODE, NDBC 41,025, and 44,004, that can approximate the flux variability associated with the GS warm waters, and the group-cold includes the three remaining NDBC buoy stations, 44,008, 44,011, and 44,018, that are located to the northwest of the GS north wall, on the colder continental shelf waters. Accordingly, Figures 14a and 14b list the three buoys of the group-warm first, followed by the three buoys of the group-cold.

[39] The mean LH of the group-warm is all above 120 Wm^{-2}, while the mean LH of the group cold does not exceed 50 Wm^{-2}. The different background air-sea conditions between the warm waters of the GS front and the colder water over the continental shelf appear to be influential. Nevertheless, at all the six buoy locations, the mean LH dominates the mean SH by a factor of 4, indicating that LH is a dominant flux component in the vicinity of the GS on the mean basis. The group-warm comparison suggests that the six flux products all overestimated the mean LH and SH

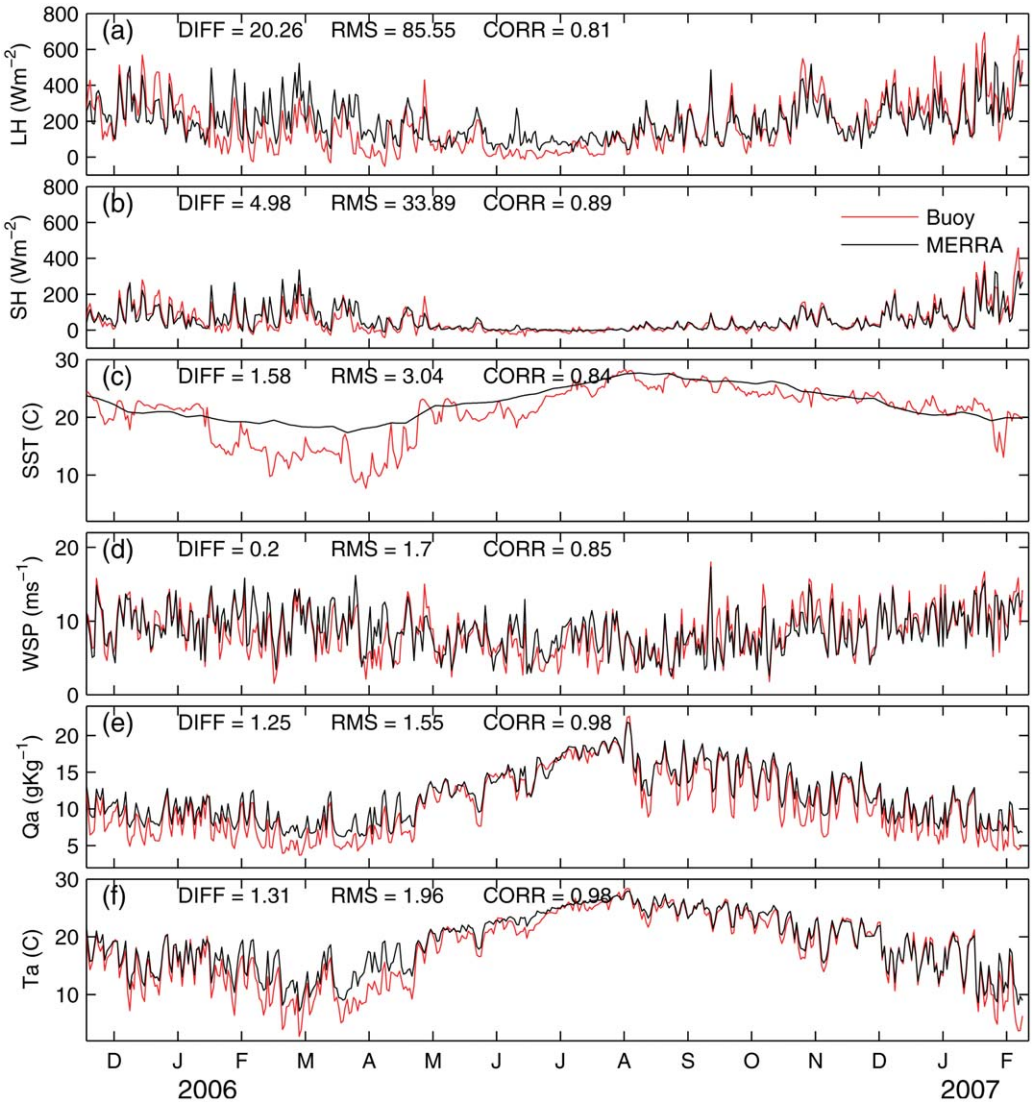

Figure 9. Same as Figure 4 but for CFSR.

at CLIMODE and NDBC 44,004. At NDBC 41,025 (upstream of CLIMODE), the six flux products differ considerably. OAFlux-0.25° LH has the best agreement with the buoy but the SH is slightly overestimated. CFSR shows an overestimation bias for LH and does a reasonable job for SH. The other four products show an underestimation at various degrees, with MERRA having the largest underestimation bias, by about 100 Wm^{-2} for LH and about 15 Wm^{-2} for SH.

[40] The group-cold comparison for LH for OAFlux-0.25°agrees well with the three buoys; all other flux products overestimate LH in the colder water zone. NCEP LH is overestimated by about 50 Wm^{-2}, which is comparable to the mean of buoy LH at these locations. NCEP SH is also overestimated and similar to LH, the magnitude of the overestimation is as large as the buoy mean SH. OAFlux-0.25° and CFSR slightly underestimate SH, while OAFlux-1° has a better agreement with buoy. MERRA and ERA-interim have good SH estimates at NDBC 44018 but slightly overestimate it at NDBC 44011.

[41] To better quantify the buoy evaluation of the flux products, the mean product-buoy differences in LH, SH, and four basic variables at each buoy location are computed for each product and then averaged over the six buoy locations. Figures 15a–15f are bar plots summarizing the mean differences for the six product-buoy pairs for six variables (LH, SH, SST, Ta, Qa, and U) averaged over the six buoy locations. Values of the three statistical properties, namely, mean differences, RMS differences, and correlation coefficient for the six product-buoy pairs are given in Tables 3 and 4.

[42] Based on Figures 15a–15f and Tables 3 and 4, the comparison of the six products with buoys can be summarized as follows.

3.3.1. Latent Heat

[43] Except for MERRA LH that is underestimated by 5.5 Wm^{-2}, all other products overestimate LH compared to

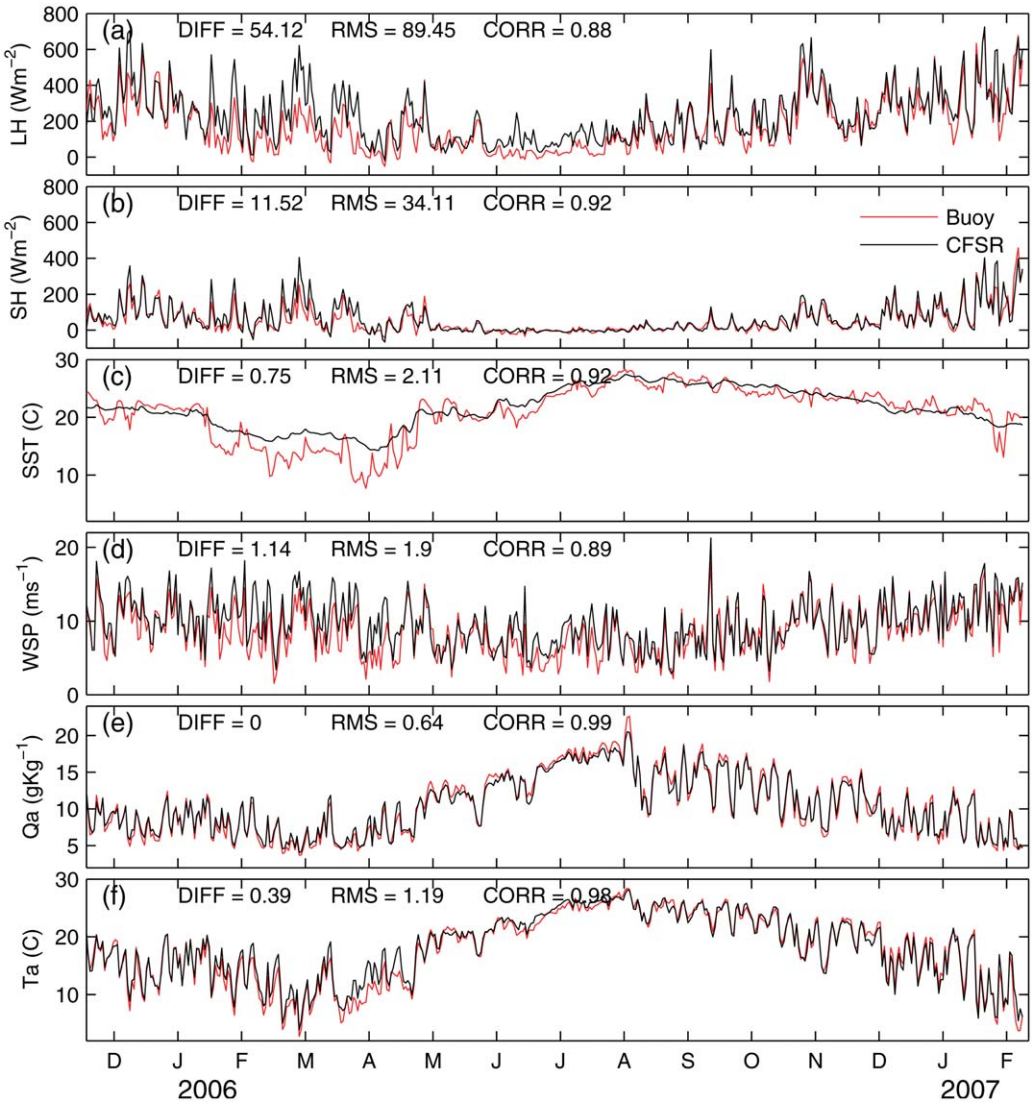

Figure 10. Same as Figure 4 but for MERRA.

the buoys. In fact, MERRA overestimates LH at the three NDBC Stations categorized under the group-cold where heat loss is low, while significantly underestimates LH at Stations 41,025 (group-warm) where heat loss is very high. The overall mean underestimation bias in MERRA LH resulted from error compensation. OAFlux*0.25° has the smallest overestimation error (7.6 Wm^{-2}), followed by OAFlux-1° (10.7 Wm^{-2}), CFSR (17.1 Wm^{-2}), ERA interim (18.9 Wm^{-2}), and NCEP (28.3 Wm^{-2}). Given that the mean LH averaged over the six buoys is 98.8 Wm^{-2}, the errors in the LH products range from 7.7% (OAFlux-0.25°) to 28.7% (NCEP) of the mean LH from buoys. OAFlux-0.25° also has the smallest RMS difference error (44.9 Wm^{-2}), followed by CFSR (49.7 Wm^{-2}), OAFlux-1° (51.5Wm^{-2}), ERA-interim (58.2 Wm^{-2}), MERRA (65.4 Wm^{-2}), and NCEP (75.4 Wm^{-2}). The correlation coefficients of the six product-buoy pairs are 0.85 and above, all significant at the 95 confidence level. If ranking the six products based on the correlation coefficient from high to low, the order would be placed as OAFlux-0.25° (0.94), CFSR (0.93), OAFlux-1° (0.91), ERA-interim (0.90), NCEP (0.86), and MERRA (0.85).

[44] Judging from the three statistical properties, OAFlux-0.25° has the best comparison with the buoy and CFSR is the second best. OAFlux-1°, though has a mean bias smaller than CFSR, has a slightly larger RMS difference error. The sensitivity of flux products to spatial resolution is hence suggested, as OAFlux-0.25°and CFSR (0.31°) are the only two products (see Table 1) that have the resolution for better resolving spatial scales of mesoscale variability associated with ocean fronts and eddies.

3.3.2. Sensible Heat

[45] The better comparison of OAFlux-0.25°and CFSR with buoys is again shown in SH. The two SH products have a near-zero mean difference from the buoys, and the highest correlation coefficients (0.95). The RMS difference error is 19.4 Wm^{-2} for OAFlux-0.25°and 21.9 Wm^{-2} for CFSR. OAFlux-1° SH is overestimated by 1.8 Wm^{-2}, but the RMS error (21.6 Wm^{-2}) and correlation coefficient (0.93) are comparable to OAFlux-0.25° and CFSR. Similar to the LH

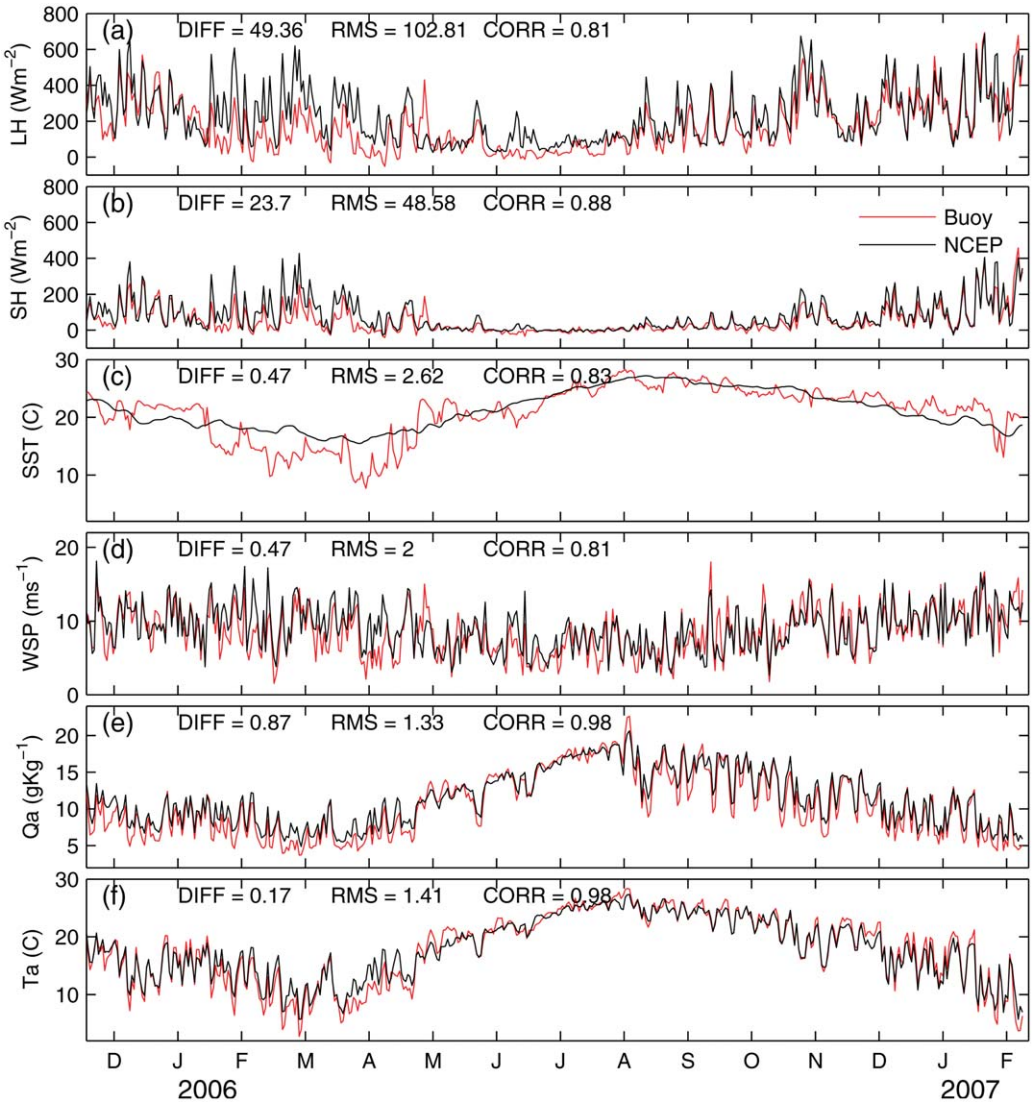

Figure 11. Same as Figure 4 but for NCEP.

comparison, MERRA SH is the only product being underestimated. Compared to the buoy mean SH of 28.3 Wm^{-2}, the mean difference error in the six products ranges from 0.0% (OAFlux-0.25°), to 0.1% (CFSR), to 6.2% (OAFlux-1°), to 5.8% (MERRA), to 8.1% (ERA-interim), and to 46.2% (NCEP). NCEP has the least favorable comparison with the buoys for both LH and SH components.

3.3.3. Basic Variables

[46] The difference errors in LH and SH result from the compensation of difference errors in SST, Qa, Ta, and U (equations (1) and (2)). The four OAFlux-0.25° basic variables represent major improvements over ERA-interim, MERRA and NCEP counterparts with respect to buoy measurements. The OAFlux-0.25° variables also improve over the OAFlux-1° counterparts. It is, therefore, not a surprise to see that OAFlux-0.25° is the best flux product at the buoy sites. Note that similar to OAFlux-0.25°, CFSR also has smaller errors in four basic variables compared to the buoy data.

[47] To complement the mean LH and SH plot in Figure 14, a Taylor diagram displaying the correlation coefficients and RMS difference errors of the six product-buoy pairs is shown in Figure 16. The OAFlux-0.25° is the best product in the group is clearly shown, along with CFSR as the second best followed by OAFlux-1°. MERRA and NCEP are less favored at the buoy locations.

4. Statistical Analysis

4.1. Wave Number Spectra and Spatial Scales

[48] Although with the resolution of 110 km, OAFlux-1° can produce a power spectrum down to 220 km at the Nyquist limit, the spectrum could be accurate only for wave length larger than at least four times the grid size, i.e., 440 km for the case of the 1° resolution. Figure 17 shows the results of spectral analysis of OAFlux-0.25° versus OAFlux-1° as well as the four reanalyses for the daily mean LH + SH in the eight winter seasons for the years 2002–2010. The spectra are calculated along meridional direction from 29°N to 45°N, covering a strip over the ocean of 1770 km, and then averaged across the basin from

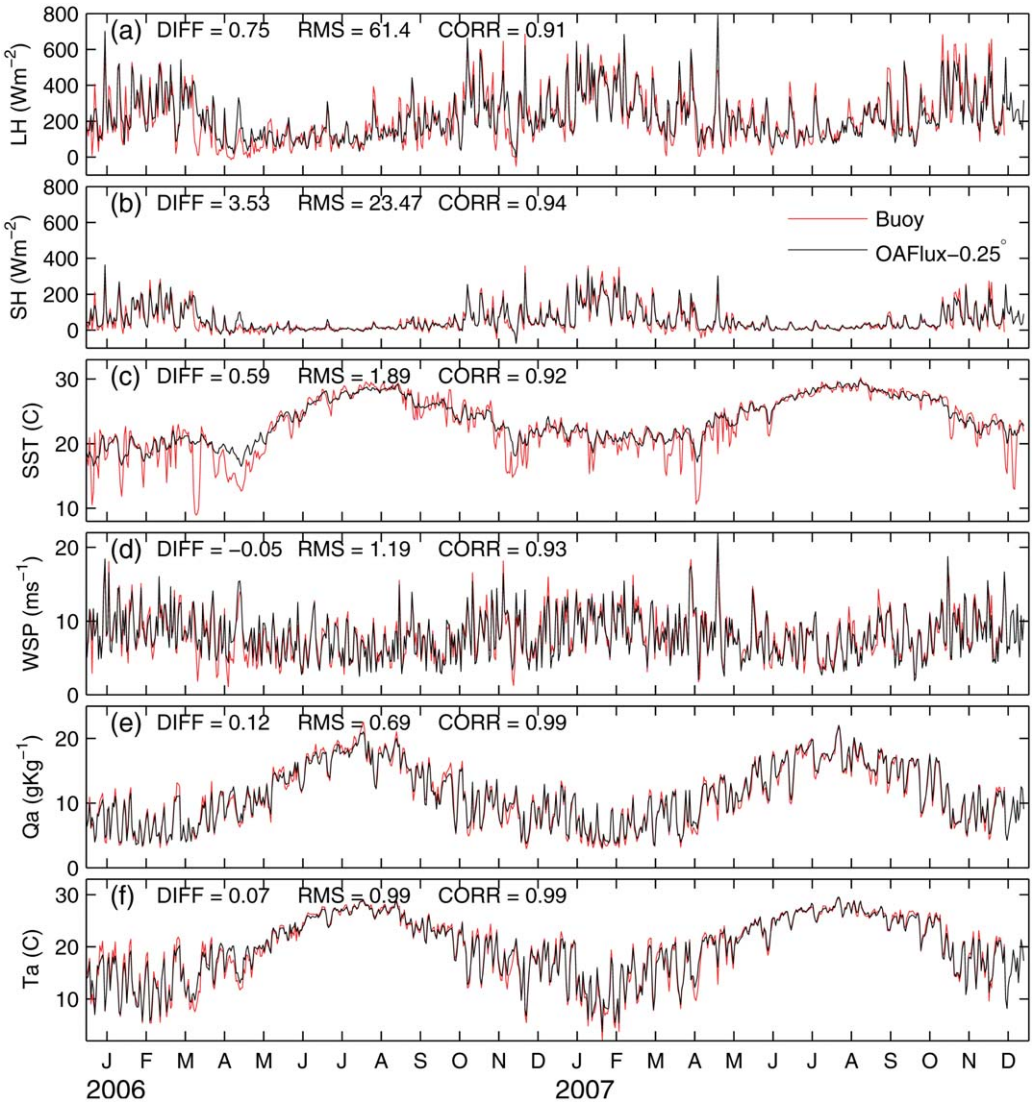

Figure 12. Same as Figure 4 but for the comparison with the NDBC buoy 41,025, located at 38.0°N, 65.0°W, for the period from January 2006 to December 2007.

75°W to 43°W. The OAFlux-0.25° LH + SH spectrum shows a roughly k^{-3} power law (Figure 17). This is different from the wave number spectra for the OAFlux-0.25° flux-related variables (i.e., SST, Ta, Qa, and U), which have the k^{-3} power law for the scale larger than 500 km and the $k^{-5/3}$ power law for the scale less than 300 km (not shown). The shape of the LH + SH spectrum, however, is found to be similar to that of (SST − Ta) and (Qs − Qa). The wave number spectrum for OAFlux-1° departs from OAFlux-0.25° falls faster at scales smaller than about 600 km, which implies the limit for an accurate description of the small-scale variability for the 1° product. For example, in comparison with OAFlux-0.25°, OAFlux-1° underestimates power spectral density (PSD) approximately 68% at scale of 300 km. Spectra from CFSR and ERA interim are similar to that from OAFlux-0.25°, but they are flatter at scale smaller than 450 km, except for a noise contribution at the smallest scales (i.e., about 70 and 150 km at the Nyquist limit for CFSR and ERA interim, respectively). The PSD from MERRA is significantly lower and the high spatial frequencies (small scales) spectrum drops even faster than the coarse-resolution NCEP. Compared to OAFlux-0.25°, the PSD from MERRA is six times smaller at scales from 250 to 350 km, indicating that OAFlux-0.25° contains much more small-scale information than MERRA.

[49] Since the length scale for the eddy variability in GS can be as short as 120 km, about four times the grid size for the 0.25° resolution, resolving air-sea flux down to the order to 0.25° is a critically important step forward in the description and understanding of the air-sea interaction. *Jiang et al*. [2012] used high-resolution shipboard measurements to examine the spatial scale of turbulent heat fluxes in Drake Passage, and estimated the decorrelation length scales of SH and LH are 65 ± 6 and 80 ± 6 km, respectively. These eddy scales are not resolved by OAFlux-1° and the reanalyses products. The decorrelation scales of SH

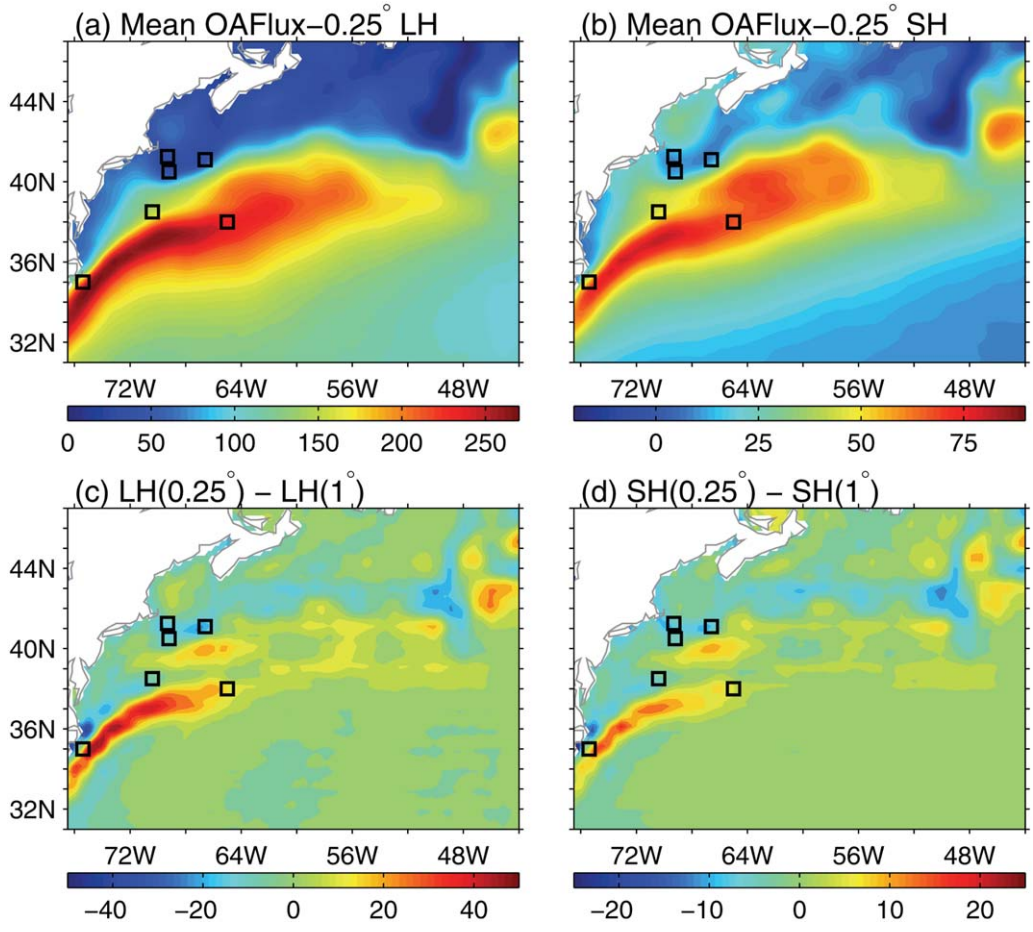

Figure 13. (a) Annual mean OAFlux-0.25° LH for the period from 2003 to 2010. (b) The same as Figure 13a but for SH. (c) The mean difference of the OAFlux-0.25° to OAFlux-1° in LH; (d) the same as Figure 13c but for SH. The square boxes indicate buoy locations. The 1° OAFlux products are linearly interpolated into 0.25° grids for comparison.

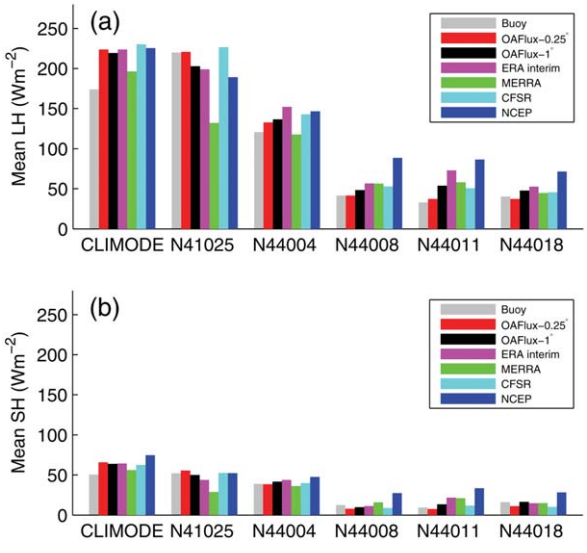

Figure 14. Bar plots of the mean averaged (a) LH and (b) SH for buoy and six products constructed using available buoy measurement periods at each of the six buoy locations.

and LH from OAFlux-1°, for example, are 118 ± 6 and 125 ± 6 km, respectively.

[50] In this study, we used the method by *Jiang et al.* [2012] to examine the decorrelation length scales of SH and LH in the GS region. The decorrelation length scale is derived by integrating the autocorrelation function with respect to the space lags from a lag of zero to the first zero crossing. The data are the same as that used for wave number spectra analysis, except LH and SH were used instead of LH + SH; in addition, the southern boundary was set at 31°N, where the first baroclinic Rossby radius is about 40 km. The results are summarized in the Table 5. The scales of SH and LH from OAFlux-0.25° are 161 ± 1 and 158 ± 1 km, and from OAFlux-1° are 183 ± 1 and 177 ± 1 km, respectively. Both ERA interim and CFSR show scales comparable with OAFlux-1°, whereas MERRA and NCEP show scales much larger than others.

[51] Note that the decorrelation length scale in OAFlux-1° is very close to the upper bound of the length scale in both the GS region (∼180 km) and the Southern Ocean (∼120 km, as the Rossby radius is less than 20 km). With a finer resolution, OAFlux-0.25° does depict eddy variability better than OAFlux-1° and the four reanalyses. For

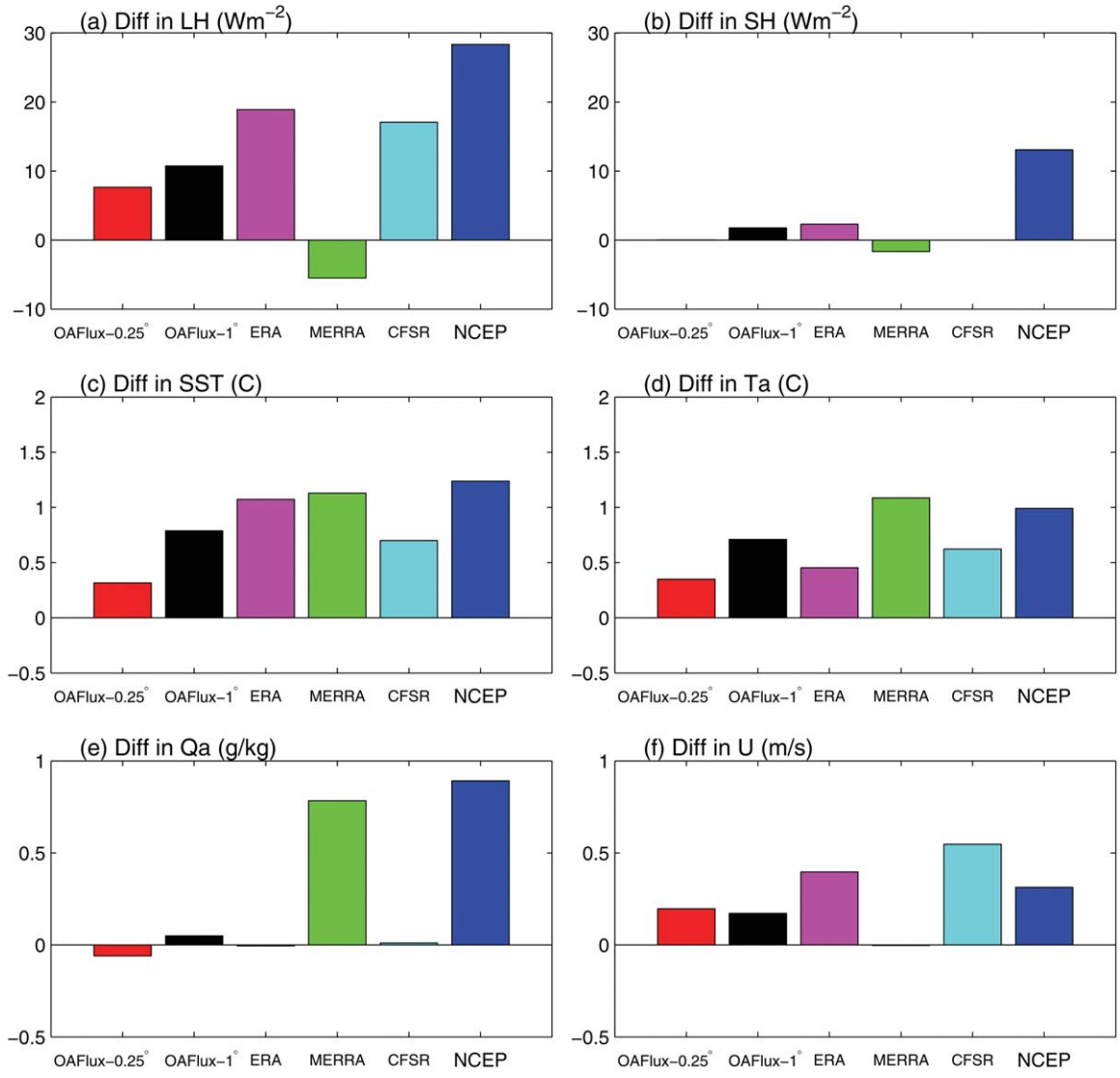

Figure 15. Mean product-buoy differences in (a) LH, (b) SH, (c) SST, (d) Ta, (e) Qa, and (f) U for the chosen six products averaged over the available buoy measurement period and then over the six buoy locations. Positive values denote the products are overestimated compared to buoy while negative values denote products are underestimated.

example, the length scale reduction is about 11% and 17% compared to OAFlux-1° and MERRA, respectively. However, in the GS region the decorrelation length scale of ~160 km from OAFlux-0.25° is in the middle but close to the upper bound of the scale (about 120–180 km) determined by the first baroclinic Rossby radius. As a result, OAFlux-0.25° still cannot resolve eddies of smaller scales.

[52] A close examination of Figure 2 can see a good example of the difference between the six participating flux products with respect to the front and eddy-like features. We chose the core regime of the GS and its extension (283–310°E, 32–42°N), calculated the deviation from the local mean (over this area) and then calculated the RMS deviation from these six data sets. The RMS of the LH + SH over the frontal area increased about 10%, i.e., from 90.3 Wm^{-2} of OAFlux-1° to 99.1 Wm^{-2}of OAFlux-0.25° (Table 6). On the other hand, CFSR has the largest RMS of 93.9 Wm^{-2}, whereas MERRA has the smallest RMS of 67.9 Wm^{-2} among the four reanalyses products.

4.2. PDF Analysis

[53] Since the buoy validations are limited to very few sites, the large-scale statistical characteristics are further evaluated in terms of PDFs. The PDFs of LH + SH from the six participating flux products, as a function of latitude, are shown in Figure 18. The PDFs were computed by using the daily mean LH + SH in the winter season for the years 2002–2010. All products agree in basic structure. The sampling distribution of heat fluxes is centered at 100 Wm^{-2} in the south and 50 Wm^{-2} in the north of the region. In the middle

Table 3. Statistics of Buoy Evaluation of OAFlux-0.25°, OAFlux-1°, and Four Atmospheric Reanalyses in LH and SH Over Six Buoys for the 2005–2007 Period[a]

	LH				SH			
	DIFF		RMS	CC	DIFF		RMS	CC
	Wm^{-2}	%	Wm^{-2}	0–1	Wm^{-2}	%	Wm^{-2}	0–1
OAFlux-0.25°	7.6	7.7	44.9	0.94	0.0	0.0	19.4	0.95
OAFlux-1°	10.7	10.9	51.5	0.91	1.8	6.2	21.6	0.94
ERA interim	18.9	19.1	58.2	0.90	2.3	8.1	23.2	0.93
MERRA	−5.5	5.6	65.4	0.85	−1.7	5.9	25.5	0.91
CFSR	17.1	17.3	49.7	0.93	−0.0	0.1	21.9	0.95
NCEP	28.3	28.7	75.4	0.86	13.1	46.2	37.2	0.91

[a]There are a total of 4288 product/buoy collocations during the three year time period. Three statistical properties are listed, including mean difference and percent (DIFF), root-mean-square (RMS) error, and correlation coefficient (cc). The mean LH and SH of the six buoys are 98.8 and 28.3 Wm^{-2}, respectively.

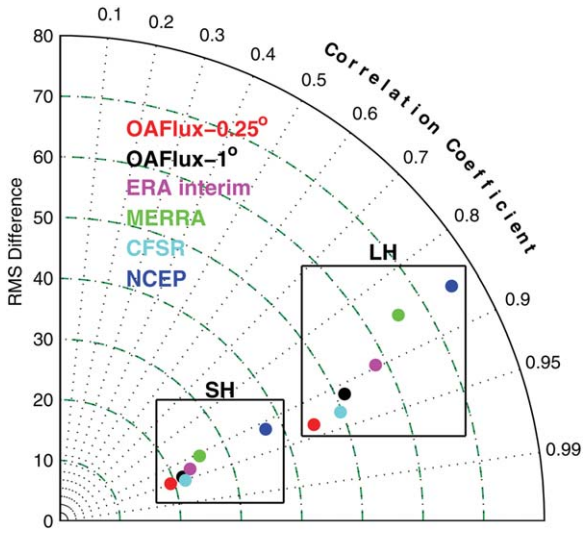

Figure 16. A Taylor diagram showing two statistical properties of the LH and SH comparison: the correlation coefficients of six pairs of products-buoy differences and RMS differences for the six pairs. A total of 4288 collocations were used in the plot.

latitudes between 35°N to 42°N, which are the locations of the maximum LH + SH front, the distributions of heat fluxes are skewed toward a more positive direction, indicating increase in the probability of strong heat loss. These statistical characteristics provide further insight into features in Figure 3 that show weaker variability in south and north (where the PDFs are more concentrated), and stronger variability in the middle latitudes (where the PDFs are decentralized). Among the six products, the distribution of heat fluxes for MERRA are more concentrated in a band between 0 and 200 Wm^{-2} along all the latitudes, whereas the distribution for NCEP tends to be more stretched out to the positive direction.

[54] The distributions of PDFs are further depicted along three selected latitudes (at 44.5°N, 38.5°N, and 32.5°N, respectively) in Figure 19. OAFlux-0.25°, OAFlux-1° and CFSR have similar distributions, featuring skewed to the right (more strong heat loss), and more leptokurtic (less variability) at high and low latitude than at middle latitude. Compared to OAFlux-0.25°, MERRA has lower probability of strong heat loss, whereas NCEP has higher probability of strong heat loss. ERA-interim has a pattern similar to OAFlux-0.25° over both cold (44.5°N) and warm (32.5°N) waters, but underestimates the probability of heat fluxes higher than 700 Wm^{-2} in the midlatitude (38.5°N), which across the core regime of the GS.

[55] Further, we compare the PDFs distribution of the daily mean LH + SH collocated from buoys and from six products, as shown in Figure 20. The results shown here are consistent with the PDFs distribution in Figure 19 that represents the characteristics for across the basin. OAFlux-0.25°, OAFlux-1°, CFSR, and ERA-interim depict similar distributions and are in good agreement with the buoys. In contrast, MERRA and NCAR exhibit a different result from the buoy. MERRA underestimates the probability of strong heat loss, which is consistent with the in situ validation from *Roberts et al.* [2012], whereas NCEP overestimates the probability of strong heat loss.

5. Summary and Conclusion

[56] The newly developed OAFlux-0.25° surface heat fluxes analysis was assessed for the eddy-rich GS region through point-to-point buoy validation and basin-scale statistical analysis in terms of wave number spectrum decorrelation of length scale, and PDFs. An intercomparison between OAFlux-0.25°, OAFlux-1°, and four atmospheric reanalyses was also performed.

Table 4. Same as Table 3 but for SST, Ta, Qa, and U

	SST			Ta			Qa			U		
	DIFF (c)	RMS (c)	CC (0–1)	DIFF (c)	RMS (c)	CC (0–1)	DIFF ($g\,Kg^{-1}$)	RMS ($g\,Kg^{-1}$)	CC (0–1)	DIFF (ms^{-1})	RMS (ms^{-1})	CC (0–1)
OAFlux-0.25°	0.32	1.35	0.98	0.35	0.97	0.99	−0.06	0.77	0.99	0.20	1.29	0.93
OAFlux-1°	0.79	1.85	0.97	0.71	1.44	0.99	0.05	0.92	0.98	0.17	1.44	0.91
ERA interim	1.07	2.16	0.96	0.45	1.24	0.99	−0.01	0.78	0.98	0.40	1.47	0.91
MERRA	1.13	2.46	0.95	1.09	1.62	0.99	0.78	1.09	0.99	−0.00	1.57	0.88
CFSR	0.70	1.80	0.97	0.62	1.25	0.99	0.01	0.67	0.99	0.55	1.28	0.94
NCEP	1.24	2.64	0.95	0.99	1.85	0.98	0.89	1.23	0.98	0.31	1.75	0.86

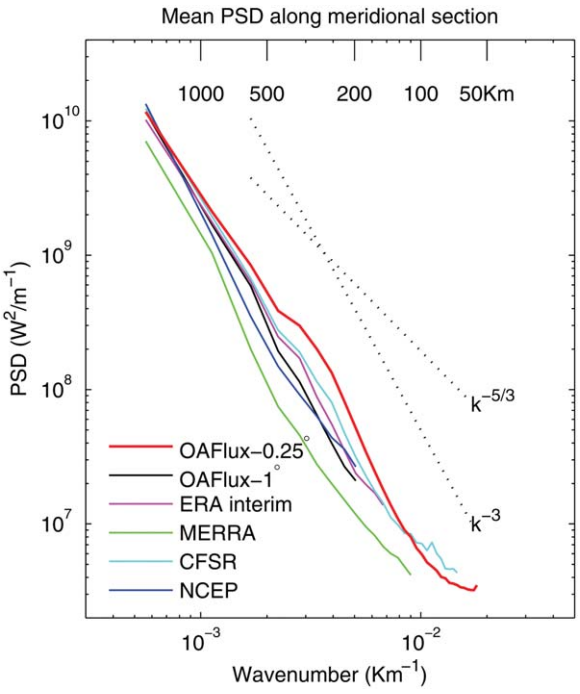

Figure 17. Log-log plots of spectra of OAFlux-0.25°, OAFlux-1°, and four reanalyses for the daily mean LH + SH. The spectra are calculated along meridional direction from 29°N to 45°N then averaged across the basin from 75°W to 43°W. Only the data of 2002 to 2010 winters (December to February) are used in this study. Dotted lines denote the slopes −3 and −5/3 for comparison.

[57] Comparison of time-mean fluxes patterns indicates that OAFlux-0.25° produces sharper and stronger fronts. The pattern of CFSR is similar to the OAFlux-0.25° counterparts, whereas MERRA underestimates ocean heat losses over the core path of the GS and overly smoothes the spatial variations. NCEP shows the smoothest and broadest pattern but has largest magnitude.

[58] Comparison of OAFlux-0.25° with CLIMODE buoy shows a reasonably good agreement in the daily mean time series over a 15 month observation period; however, OAFlux-0.25° heat fluxes are overestimated, in particular during the winter season. The cause of such overestimate is primarily due to a mismatch in SST between gridded data and point measurements when strong spatial gradients are presented. At NDBC Station 41,025, which is located in a key point to measure the GS fronts, OAFlux-0.25° compares very well with buoy measurements, indicating a major improvement over OAFlux-1° in resolving the heat fluxes in the vicinity of sharp oceanic fronts. Over the three NDBC Stations located in the cold water north of the GS, OAFlux-0.25° has nearly a perfect match in both LH and SH compared to buoy counterparts.

[59] In comparison with OAFlux-1° and the four reanalyses, OAFlux-0.25° has the best performance with respect to buoy observations in both LH and SH. The mean biases in LH and SH for OAFlux-0.25° over the six buoys are 7.6 Wm^{-2} (7.7%) with RMS error of 44.9 Wm^{-2}, and 0.0 Wm^{-2} with RMS error of 19.4 Wm^{-2}, respectively. CFSR is the second best, followed by OAFlux-1°. MERRA has smaller mean bias in both LH and SH but lager RMS error in comparison with ERA-interim and CFSR. NCEP is less favored in comparison with buoy observations.

[60] The wave number spectrum for the OAFlux-0.25° LH + SH shows a roughly k^{-3} power law. The spectrum for OAFlux-1° departs from OAFlux-0.25° at scales about 600 km, implying that the 1° product is less representative of variability with the length scale less than this limit. Comparison among the six products shows that higher resolution product contains more small-scale information, except for MERRA of which the PSD is significantly lower overall and the high spatial frequency spectrum drops even faster than the coarse-resolution NCEP. The decorrelation length scale analysis indicates that OAFlux-0.25° depicts eddy variability better than OAFlux-1° and the four reanalyses; however, its capability in detecting eddies with smaller scale still needs to be improved.

[61] The meridional distribution of PDFs of LH + SH indicates that the large-scale spatial patterns from the six products are generally in agreement with each other. In the latitude band between 35°N and 42°N, the distributions of LH + SH are skewed toward a more positive direction, showing evidence for strong oceanic heat loss along the core of the GS. Despite the similarity in structure, MERRA shows lower probability of strong heat loss, whereas NCEP shows higher probability of strong heat loss, in comparison with the others. ERA-interim closely resembles the distribution for OAFlux-0.25° over both cold and warm waters, but it underestimates the probability of heat fluxes higher than 700 Wm^{-2} in the midlatitude across the core regime of the GS. The PDFs distributions in terms of the data collocated from buoys and the six products are found to be consistent with the PDFs characteristics for across the basin.

[62] Among the four reanalyses, CFSR stands out as the best in comparison with OAFlux-0.25°. CFSR has the highest resolution (0.31°) for better resolving the small-scale variability; it also has overall best quality in flux-related variables, and that leads to smaller errors in heat fluxes, with respect to buoy observations.

Table 5. Decorrelation Length Scales of SH and LH From the Six Products[a]

Product	OAFlux-0.25°	OAFlux-1°	ERA Interim	MERRA	CFSR	NCEP
SH scale (km)	161 ± 1	183 ± 1	179 ± 1	197 ± 1	181 ± 1	206 ± 1
LH scale (km)	158 ± 1	177 ± 1	177 ± 1	187 ± 1	174 ± 1	198 ± 1

[a]The data used in the calculation are as the same as that used for the wave number spectra, except LH and SH were used instead of LH + SH; in addition, the southern boundary was set at 31°N. Error bars are two times standard error.

Table 6. The RMS Deviation of LH + SH From the Local Mean Over an Area Within the Core of the GS (283–310°E, 32–42°N)[a]

Product	OAFlux-0.25°	OAFlux-1°	ERA Interim	MERRA	CFSR	NCEP
RMS (Wm^{-2})	99.1	90.3	78.4	67.9	93.9	79.2

[a]The mean LH + SH of eight winter season from December 2002 to February 2010 was used in the calculation.

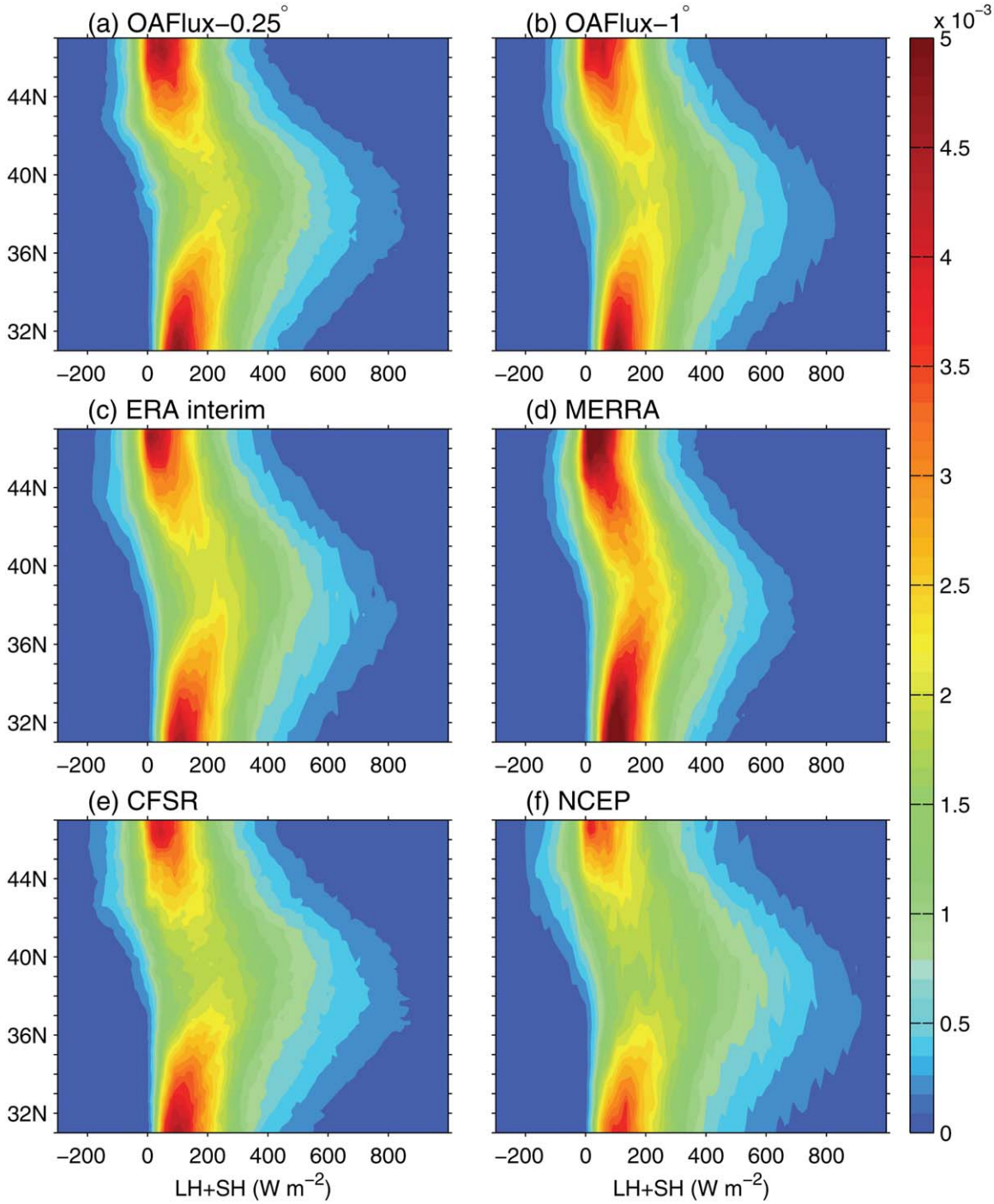

Figure 18. PDFs of the daily mean LH + SH as a function of latitude from (a) OAFlux-0.25°, (b) OAFlux-1°, (c) ERA interim, (d) MERRA, (e) CFSR, and (d) NCEP. PDFs are computed by combining LH + SH over the ocean from all longitudes over the 8 year winter time period from December 2002 to February 2010.

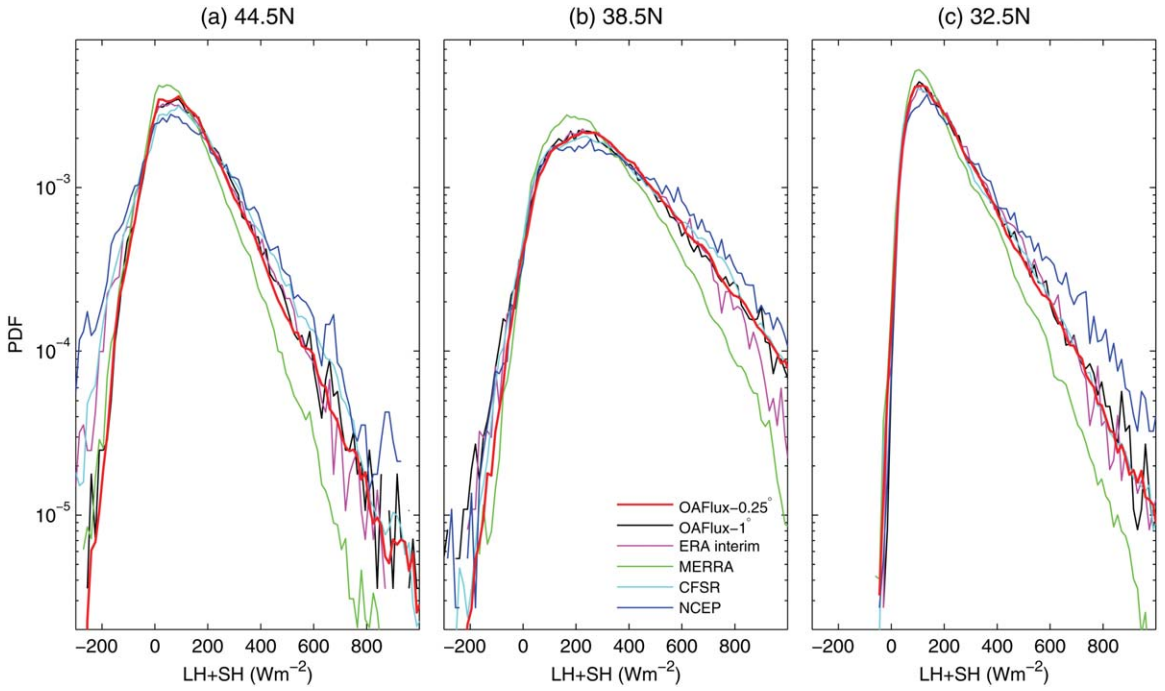

Figure 19. PDFs of the daily mean LH + SH along (a) 44.5°N, (b) 38.5°N, and (c) 32.5°N from the six products. The PDFs are calculated as the same as the ones in Figure 18.

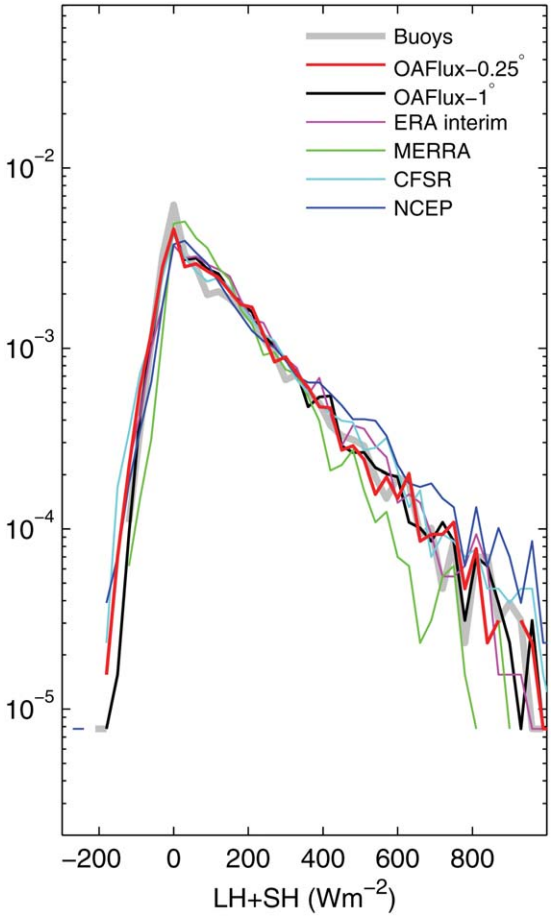

Figure 20. Comparison of PDFs of the daily mean LH + SH, which are collocated from buoys and six products, over the 3 year time period from 2005 to 2007.

[63] **Acknowledgments.** This study was supported by NOAA Ocean Climate Observations program (OCO) under grant NA09OAR4320129 and the NASA Ocean Vector Wind Science Team (OVWST) under grant NNA10AO86G. We thank Darren Jackson and Gary Wick for providing satellite-derived air temperature and humidity, and Sebastien Bigorre for providing CLIMODE buoy measurements. The NDBC buoy measurements were obtained from http://www.ndbc.noaa.gov. ERA-interim, CFSR, and NCEP reanalyses were downloaded from the NCAR Research Data Archive at http://rda.ucar.edu, MERRA was downloaded from the Global Modeling and Assimilation Office (GMAO) and the GES DISC at ftp://goldsmr2.sci.gsfc.nasa.gov.

References

Andersson, A., C. Klepp, K. Fennig, S. Bakan, H. Grassl, and J. Schulz (2011), Evaluation of HOAPS-3 ocean surface freshwater flux components. *J. Appl. Meteorol. Climatol.*, *50*, 379–398.

Bentamy A., K. B. Katsaros, M. Alberto, W. M. Drennan, E. B. Forde, and H. Roquet (2003), Satellite estimates of wind speed and latent heat flux over the global oceans, *J. Clim.*, *16*, 637–656.

Bigorre, S., R. Weller, J. Edson, and J. Ware (2013), A surface mooring for air-sea interaction research in the Gulf Stream. Part 2: Analysis of the observations and their accuracies, *J. Atmos. Oceanic Technol.*, *30*, 450–469, doi:10.1175/JTECH-D-12–00078.1.

Bourras, D. (2006), Comparison of five satellite-derived latent heat flux products to moored buoy data. *J. Clim.*, *19*, 6291–6313, doi:10.1175/JCLI3977.1.

Chelton, D. B., and F. J. Wentz (2005), Global microwave satellite observations of sea surface temperature for numerical weather prediction and climate research, *Bull. Am. Meteorol. Soc.*, *86*, 1097–1115.

Chelton, D. B., R. A. deSzoeke, M. G. Schlax, K. E. I. Naggar, and N. Siwertz (1998), Geographical variability of the first baroclinic Rossby radius of deformation, *J. Phys. Oceanogr.*, *28*, 433–460.

Colbo, K., and R. A. Weller (2009), The accuracy of the IMET sensor package in the subtropics, *J. Atmos. Oceanic Technol.*, *9*, 1867–1890.

Cronin, M. F., et al. (2010), Monitoring ocean-atmosphere interactions in western boundary current extensions, *Proceedings of the "Ocean-Obs'09: Sustained Ocean Observations and Information for Society" Conference*, Vol. 2, *ESA Publication WPP-306*, edited by J. Hall, D. E. Harrison, and D. Stammer, Venice, Italy, September 2009, doi:10.5270/OceanObs09.cwp.20.

Davis X. J., R. A. Weller, S. Bigorre, and A. J. Plueddemann (2013), Local oceanic response to atmospheric forcing in the Gulf Stream Region, *Deep Sea Res., Part II*, *91*, 71–83.

Dee, D. P., et al. (2011), The ERA-Interim reanalysis: Configuration and performance of the data assimilation system. *Q. J. R. Meteorol. Soc.*, *137*, 553–597. doi:10.1002/qj.828.

Fairall, C. W., E. F. Bradley, J. E. Hare, J. E., A. A. Grachev, and J. B. Edson (2003), Bulk parameterization of air-sea fluxes: Updates and verification for the COARE algorithm, *J. Clim.*, *16*, 571–591.

Gulev, S. K., and K. Belyaev (2012), Probability distribution characteristics for surface air–sea turbulent heat fluxes over the global ocean, *J. Clim.*, *25*, 184–206.

Jackson, D. L., and G. A. Wick (2010), Near-surface air temperature retrieval derived from AMSU-A and sea surface temperature observations, *J. Atmos. Oceanic Technol.*, *27*, 769–1776.

Jackson, D. L., G. A. Wick, and J. J. Bates (2006), Near-surface retrieval of air temperature and specific humidity using multi-sensor microwave satellite observations, *J. Geophys. Res.*, *111*, D10306, doi:10.1029/2005JD006431.

Jackson, D. L., G. A. Wick, and F. R. Robertson (2009), Improved multisensor approach to satellite-retrieved near-surface specific humidity observations, *J. Geophys. Res.*, *114*, D16303, doi:10.1029/2008JD011341.

Jiang, C. L., S. T. Gille, J. Sprintall, K. Yoshimura, and M. Kanamitsu (2012), Spatial variation in turbulent heat fluxes in drake passage, *J. Clim.*, *25*, 1470–1488. doi:10.1175/2011JCLI4071.1.

Kalnay, E., et al. (2006), The NCEP/NCAR 40-year reanalysis project, *Bull. Am. Meteorol. Soc.*, *77*, 437–471.

Kanamitsu, M., W. Ebisuzaki, J. Woollen, S.-K. Yang, J. J. Hnilo, M. Fiorino, and G. L. Potter (2002), NCEP-DOE AMIP-II Reanalysis (R-2), *Bull. Am. Meterol. Soc.*, *83*, 1631–1643.

Kelly, K. A., R. J. Small, R. M. Samelson, B. Qiu, T. M. Joyce, Y.-O. Kwon, and M. F. Cronin, (2010), Western boundary currents and frontal air sea interaction: Gulf Stream and Kuroshio Extension, *J. Clim.*, *23*, 5644–5667.

Kubota, M., N. Iwasaka, S. Kizu, M. Konda, and K. Kutsuwada (2002), Japanese ocean flux data sets with use of remote sensing observations (J-OFURO), *J. Oceanogr.*, *58*, 213–225.

Liu, W. T. and W. Tang (1996), *Equivalent Neutral Wind, JPL Publication 96-17*, 16 pp., Jet Propul. Lab., Pasadena, Calif.

Marshall, J., et al. (2009), Observing the cycle of convection and restratification over the Gulf Stream system and the subtropical gyre of the North Atlantic Ocean: Preliminary results from the CLIMODE field campaign, *Bull. Am. Meteorol. Soc.*, *90*, 1337–1350.

Milliff, R. F., J. Morzel, D. B. Chelton, and M. H. Freilich (2004), Wind stress curl and wind stress divergence biases from rain effects on QSCAT surface wind retrievals, *J. Atmos. Oceanic Technol.*, *21*, 1216–1231.

Minobe, S., A. Kuwano-Yoshida, N. Komor, S.-P. Xie, and R. J. Small (2008), Influence of the Gulf Stream on the troposphere, *Nature*, *452*, 206–209.

National Data Buoy Center (2013), Frequently Asked Questions (FAQ): What are the sensors' reporting, sampling, and accuracy readings? [Available at http://www.ndbc.noaa.gov/rsa.shtml.]

Reynolds, R. W., T. M. Smith, C. Liu, D. B. Chelton, K. S. Casey, and M. G. Schlax (2007), Daily high-resolution blended analyses for sea surface temperature, *J. Clim.*, *20*, 5473–5496.

Rienecker, M. M., et al. (2011), MERRA: NASA's modern-era retrospective analysis for research and applications, *J. Clim.*, *24*, 3624–3648.

Roberts, J. B., F. R. Robertson, C. A. Clayson, and M. G. Bosilovich (2012), Characterization of turbulent latent and sensible heat flux exchange between the atmosphere and ocean in MERRA, *J. Clim.*, *25*, 821–838, doi:10.1175/JCLI-D-11–00029.1.

Saha, S., et al. (2010), The NCEP climate forecast system reanalysis, *Bull. Am. Meteorol. Soc.*, *91*, 1015–1057.

Shie, C.-L., K. Hilburn, L. S. Chiu, R. Adler, I-I. Lin, E. Nelkin, J. Ardizzone, and S. Gao (2012), *Goddard Satellite-Based Surface Turbulent Fluxes, Daily Grid, version 3*, edited by A. Savtchenko, Goddard Earth Sci. Data and Inf. Serv. Cent., Greenbelt, Md., doi:10.5067/MEASURES/GSSTF/DATA301. [Available at doi:10.5067/MEASURES/GSSTF/DATA301.]

Small, R. J., S. P. DeSzoeke, S. P. Xie, L. O'Neill, H. Seo, Q. Song, P. Cornillon, M. Spall, and S. Minobe (2008), Air-sea interaction over ocean fronts and eddies, *Dyn. Atmos. Oceans*, *45*, 274–319, doi:10.1016/j.dynatmoce.2008.01.00.

Sweet, W., R. Fett, J. Kerling, and P. La Violette (1981), Air-sea interaction effects in the lower troposphere across the north wall of the Gulf Stream, *Mon. Weather Rev.*, *109*, 1042–1052.

Uppala, S. M., et al. (2005), The ERA-40 re-analysis, *Q. J. R. Meteorol. Soc.*, *131*, 2961–3012.

Vogelzang, J., A. Stoffelen, A. Verhoef, and J. Figa-Saldana (2011), On the quality of high-resolution scatterometer winds, *J. Geophys. Res.*, *116*, C10033, doi:10.1029/2010JC006640.

Wallace, J. M., T. P., Mitchell, and C. Deser (1989), The influence of sea surface temperature on surface wind in the eastern equatorial Pacific: Seasonal and interannual variability, *J. Clim.*, *2*, 1492–1499.

Weller, R. A., P. B. Sebastien, J. Lord, J. D. Ware, and J. B. Edson (2012), A surface mooring for air–sea interaction research in the Gulf Stream. Part I: Mooring design and instrumentation, *J. Atmos. Oceanic Technol.*, *29*, 1363–1376. doi:10.1175/JTECH-D-12–00060.1.

Williams, R., C. Wilson, and C. W. Hughes (2007), Ocean and atmosphere storm tracks: The role of eddy vorticity forcing, *J. Phys. Oceanogr.*, *37*, 2267–2289.

Wunsch, C. (2002), Ocean observations, the climate forecast problem, in *Meteorology at the Millennium*, edited by R. P. Pearce, pp. 233–245, Academic, London.

Yu, L., R. A. Weller, and B. Sun (2004a), Improving latent and sensible heat flux estimates for the Atlantic Ocean (1988–1999) by a synthesis approach, *J. Clim.*, *17*, 373–393.

Yu, L., R. A. Weller, and B. Sun (2004b), Mean and variability of the WHOI daily latent and sensible heat fluxes at in situ flux measurement sites in the Atlantic Ocean, *J. Clim.*, *17*, 2096–2118.

Yu, L., X. Jin, and R. A. Weller (2008), Multidecade global flux datasets from the objectively analyzed air-sea fluxes (OAFlux) Project: Latent and sensible heat fluxes, ocean evaporation, and related surface meteorological variables, *OAFlux Proj. Tech. Rep. OA-2008-01,* 64 pp., Woods Hole Oceanogr. Inst., Woods Hole, Mass.

Yu, L. K., and X. Jin (2012), Buoy perspective of a high-resolution global ocean vector wind analysis constructed from passive radiometers and active scatterometers (1987–present), *J. Geophys. Res.*, *117*, C11013, doi:10.1029/2012JC008069.